International Journal of Fatigue 178 (2024) 108024

Contents lists available at ScienceDirect

International Journal of Fatigue

journal homepage: www.elsevier.com/locate/ijfatigue

Low cycle fatigue behaviour of cellular materials: Experimental comparative study of strut-based and gyroid structures made of additively manufactured 316L steel

Marco Pelegatti [a,*], Federico Scalzo [a], Francesco Sordetti [a], Emanuele Vaglio [a], Michele Magnan [a], Giovanni Totis [a], Marco Sortino [a], Denis Benasciutti [b], Alex Lanzutti [a], Francesco De Bona [a], Enrico Salvati [a]

[a] Polytechnic Department of Engineering and Architecture, University of Udine, via delle Scienze 208, 33100 Udine, Italy
[b] Department of Engineering, University of Ferrara, via Saragat 1, 44122 Ferrara, Italy

ARTICLE INFO

Keywords:
Cellular materials
Lattice structures
Laser-powder bed fusion
316L stainless steel
Low cycle fatigue

ABSTRACT

Cellular materials are an attractive option to improve mechanical properties in lightweight design. Given their complex geometry, cellular materials present small features at the meso-scale that make them highly susceptible to fatigue failures. Fatigue of these materials has been receiving adequate attention only in the last few years, nevertheless, studies of low cycle fatigue (LCF) behaviour are extremely scarce and fragmented. In this study, 316L steel strut-based (FBCCZ) and gyroid cellular specimens were successfully manufactured by laser-powder bed fusion and tested in the LCF regime, considering their post-manufacturing morphological characteristics. The cyclic elastoplastic response revealed a higher stiffness for the strut-based than the gyroid cellular structure. The latter, in contrast, exhibited higher fatigue strength in strain-control mode, thanks to the absence of severe stress and strain raisers when compared to the strut-based counterpart. Overall, strain-life curves of both types of cellular materials are shifted to lower number of cycles to failure with respect to the base material. Detailed fractographic analyses revealed complex and tri-dimensional fracture surfaces for the gyroid specimens, whereas the strut-based lattice displayed planar fracture surfaces.

1. Introduction

Cellular, or lattice, materials are structured materials based on a periodic arrangement of a regular unit cell in space [1,2]. Additive manufacturing (AM) is the most suitable manufacturing process to produce such complex structures at a very small scale and with good quality. Other manufacturing processes can fabricate two-dimensional or relatively simple three-dimensional structures, though with less control. The first classification of cellular structures based on the geometry of the unit cell is between open and closed cell porosity. A further distinction can be made between strut-based [3] and triply periodic minimal surfaces- (TPMS-) based cellular structures [4]. The unit cell of strut-based cellular structures is composed of struts and nodes, whereas TPMS-based is obtained from a surface that divides the space into two parts. From that starting surface, two types of unit cells are defined: sheet-TPMS and skeletal-TPMS. Unit cells of sheet-TPMS cellular structures are obtained by thickening the initial surface, whereas skeletal-TPMS are obtained by defining one of the two regions of the space as solid.

From a practical point of view, cellular structures are intricate geometries manufactured at a small scale to fill the geometry at the component scale. Therefore, the macroscopic behaviour of the component is ruled by the topology of the unit cell and its spatial distribution, in the same way as the mechanical response of a part changes by choosing different materials. For this reason, cellular structures are also called cellular or lattice *materials*. The main advantage of cellular structures is, therefore, to tune the mechanical properties of components by changing the topology of the unit cell and its relative density (i.e., porosity). Furthermore, cellular materials can always lighten components thanks to the fact that they use only a minimal quantity of material. Considering this design versatility, cellular structures have been proposed in different applications, as accurately reviewed by Du Plessis

* Corresponding author.
E-mail address: pelegatti.marco@spes.uniud.it (M. Pelegatti).

https://doi.org/10.1016/j.ijfatigue.2023.108024
Received 8 September 2023; Received in revised form 18 October 2023; Accepted 23 October 2023
Available online 25 October 2023

et al. [5]. Structural properties are relevant in many of them, such as in impact and energy absorbers [6,7], vibration damping [8,9,10] and in lightweight components in general [11,12]. Cellular materials are also well suited to tune thermal properties in heat transfer systems [13] and stiffness and permeability for osseointegration in biomedical prostheses [14]. This extended usability of cellular structures makes them attractive in many industrial sectors, from aerospace and automotive to biomedical and electronic fields [15,16,17].

For the above reasons, the mechanical behaviour of cellular materials has been the focus of many studies. Static properties were widely investigated under several loading conditions, ranging from compression [18,19] and tension [20] to torsion [21] and shear [22], using both experimental and numerical methods. Mechanical properties, such as elastic modulus, yield strength and ultimate tensile strength were related to the topology of the unit cell, relative density and base material [23]. These parameters are considered the most influential in designing components with cellular structures. Anisotropy of cellular materials is another relevant feature that has been widely studied in quasi-static loading conditions [24,25].

More recently, the fatigue performance of these materials has attracted the interest of many researchers and engineers. However, only compression-compression fatigue response has been widely covered at first [26,27,28,29]. This is mainly due to a number of experimental challenges encountered when testing these materials in the tensile regime. Nevertheless, the scientific community has recognised the relevance of extending this knowledge to a broader range of fatigue loading conditions. At the same time, increasing confidence in the experimental setup for fatigue testing has been achieved, and different authors proposed a variety of specimens designed for fatigue tests in tension with successful results [30,31,32,33]. Works on fatigue properties under different load ratios [34] and random loading can now be found in the literature [35]. Also, fatigue crack propagation in lattice structures was studied by Li et al. [36]. Nonetheless, all these studies on fatigue are conducted in the high cycle fatigue (HCF) regime in load control, whereas low cycle fatigue (LCF) and the cyclic elastoplastic response have not been investigated by experimental tests yet, to the best of the authors' knowledge. Only a couple of works by Tomažinčič et al. constitute an exception, where experiments and numerical simulations are assessed to characterise the cyclic response and fatigue strength [37,38]. However, the cellular structures studied in these works are essentially two-dimensional and were produced by water-jetting starting from rolling sheets of Al alloy. On the other hand, the low cycle fatigue behaviour of three-dimensional cellular structures was studied by very few works using an exclusively numerical approach. For example, Molavitabrizi et al. established a computational approach to predict fatigue strain-life curves for two different unit cells by combining elastoplastic homogenisation and the theory of critical distance [39]. A similar framework was proposed by Mozafari et al. to predict the fatigue life of cellular structures covering the HCF and LCF regime but using local plastic strain energy density in a cycle as a fatigue indicator parameter [40]. A different method to predict the LCF behaviour of diamond and gyroid cellular structures was proposed by Zhang et al., who used a cyclic plasticity model coupled with damage to obtain the cyclic response and fatigue strength of the whole cellular structure [41]. In the meantime, LCF properties of additively manufactured bulk metals have been extensively characterised in the last years, differently from the cellular materials. These studies covered a wide range of metallic materials that are considered suitable to be manufactured by AM systems, such as AISI 316L steel [42,43,44,45], Ti6Al4V [46,47] and Inconel 718 [48,49].

The current study aims to extend the knowledge of the fatigue behaviour of cellular materials at LCF loading conditions from an experimental point of view. This knowledge could expand the range of applications to more severe strain control loading conditions, such as in the case of components subjected to thermo-mechanical loads in the aerospace industry or vibration dampers. In this work, cellular specimens made of AISI 316L steel are designed to be loaded in cyclic tension–compression in strain-control mode and manufactured by laser-powder bed fusion (L-PBF). The majority of the studies about the fatigue of cellular structures regard Ti6Al4V alloy, whereas L-PBF 316L steel has been considered mainly in works on static behaviour [50,51,52,53,54,55]. Therefore, this study also aims to enrich the current literature in this area. In addition, two cellular structures are considered in the investigation: a strut-based unit cell, called FBCCZ, and a TPMS-based unit cell, namely skeletal-gyroid. The two types of lattice cells are expected to provide different mechanical properties in terms of stress–strain hysteresis loops and fatigue strength and, therefore, suggest use under different operating conditions. Morphologies of the fracture surfaces were also examined to characterise the damage mechanisms of cellular materials during cycling.

2. Materials and methods

2.1. Base material and cellular specimens

Two different unit cell topologies were considered in this work. The first one is a strut-based lattice cell called FBCCZ [18], which combines the face-centred cubic (FCC) and body-centred cubic (BCC) cells with the addition of four vertical struts along the z-direction (see Fig. 1 (a)). The number of nodes and struts in the cell makes the mechanical behaviour of this topology bending-dominated based on the Maxwell stability criterion [56]. However, if this cell is loaded along the z-direction, it is experimentally demonstrated that the response is basically stretching-dominated [18,57]. The considered cell is 2 mm per side, with the diameter of the struts equal to 0.4 mm. These dimensions lead to a ratio of the volume occupied by the solid material V_{solid} to the total volume occupied by the cell V_{tot}, or relative density $\bar{\rho}$ [1], of about 31 %, according to:

$$\bar{\rho} = \frac{\rho^*}{\rho_s} = \frac{V_{solid}}{V_{tot}} \tag{1}$$

where ρ^* and ρ_s are the density of the cellular and base material, respectively.

The second unit cell is a skeletal-TPMS (or network-TPMS). TPMS includes a variety of geometries, among which the gyroid is probably the mostly employed one and thus chosen for this study. Interested readers can learn more about TPMS and gyroid in the references [4,58]. For the sake of brevity, the main aspects of the gyroid cell studied in this work are summarised in the following. As mentioned in the Introduction, the skeletal-gyroid cell is generated by starting from the gyroid surface that separates the space into two regions. The gyroid surface can be approximately determined by finding $U(x,y,z) = 0$ of the function [59]:

$$\begin{aligned} U(x,y,z) = & sin\left(\frac{2\pi}{l_0}x\right)cos\left(\frac{2\pi}{l_0}y\right) + sin\left(\frac{2\pi}{l_0}y\right)cos\left(\frac{2\pi}{l_0}z\right) \\ & + sin\left(\frac{2\pi}{l_0}z\right)cos\left(\frac{2\pi}{l_0}x\right) - t \end{aligned} \tag{2}$$

Then, the skeletal-gyroid cell can be obtained by filling with solid material the region of the space where $U(x,y,z) \leq 0$. The parameter l_0 is the size of the unit cell, whereas t is a constant which rules the relative density of the cellular material. In order to fairly compare the behaviour of the gyroid with the FBCCZ cell, the relative density was chosen to be the same (i.e. 31 %), which is obtained by imposing $t = -0.57$ in Eq. (2). The size of the cell is selected to be 2 mm, equal to the FBCCZ structure. Fig. 1 (b) depicts the studied gyroid unit cell. The skeletal-gyroid geometry is not directly composed of nodes and struts, which excludes the use of the Maxwell stability criterion to predict the mechanical behaviour. Nevertheless, the geometry can be schematised by nodes and struts, as reported in [60]. This approximation yields a correct prediction of the mechanical properties as long as the relative density is low (i.e. less than 15 %) because of the continuous curvature between the

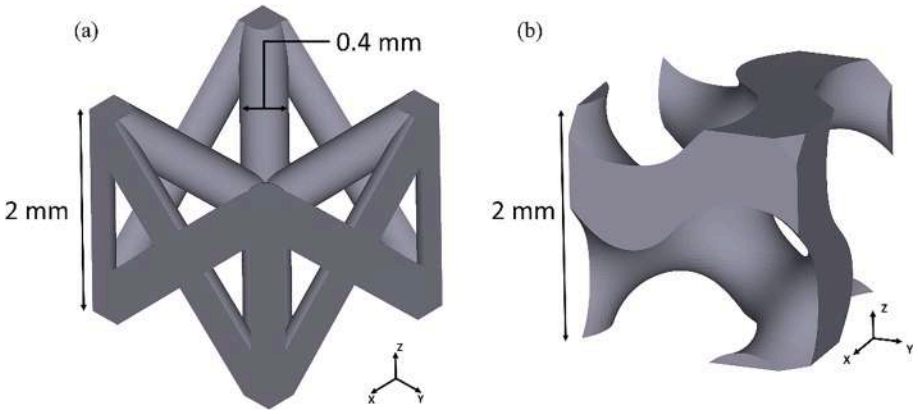

Fig. 1. Unit cell topologies and dimensions: (a) FBCCZ and (b) skeletal-gyroid.

"pseudo-struts" and "pseudo-nodes" of the real geometry. Nonetheless, the results obtained by Yang et al. suggest that the skeletal-gyroid has an overall bending-dominated response [60].

The specimen geometry for both the FBCCZ and gyroid cells is reported in Fig. 2 (a-b). The design of fatigue cellular specimens is not trivial due to several challenges, such as avoiding invalid failures during fatigue tests. The cellular part has 6 × 6 × 19 cells, with 15 rows of cells in the middle of the specimens with a constant relative density of about 31 %. The smooth transition of two rows between the solid and cellular parts, reported in Fig. 2 (a-b), was designed with an increasing relative density. This expedient reduces the possibility of failure outside the gauge length of the specimen, as suggested in [52,61]. Furthermore, 6 × 6 cells in the transversal section of the specimen mitigate the edge effects enough and allow the mechanical response to be representative of the cellular material. Other authors suggested using a minimum number of 7 cells in the cross-section [62]. However, 6 cells were eventually selected because of size limitations due to the experimental equipment. In any case, preliminary finite element simulations proved that the difference in the stress–strain response between a row of 6 × 6 and 7 × 7 cells is negligible in the explored range of strains of the present study [63].

The total axial length of the specimens is 128 mm, including 45 mm of the grip portion for each side. The cross-section in the cellular part

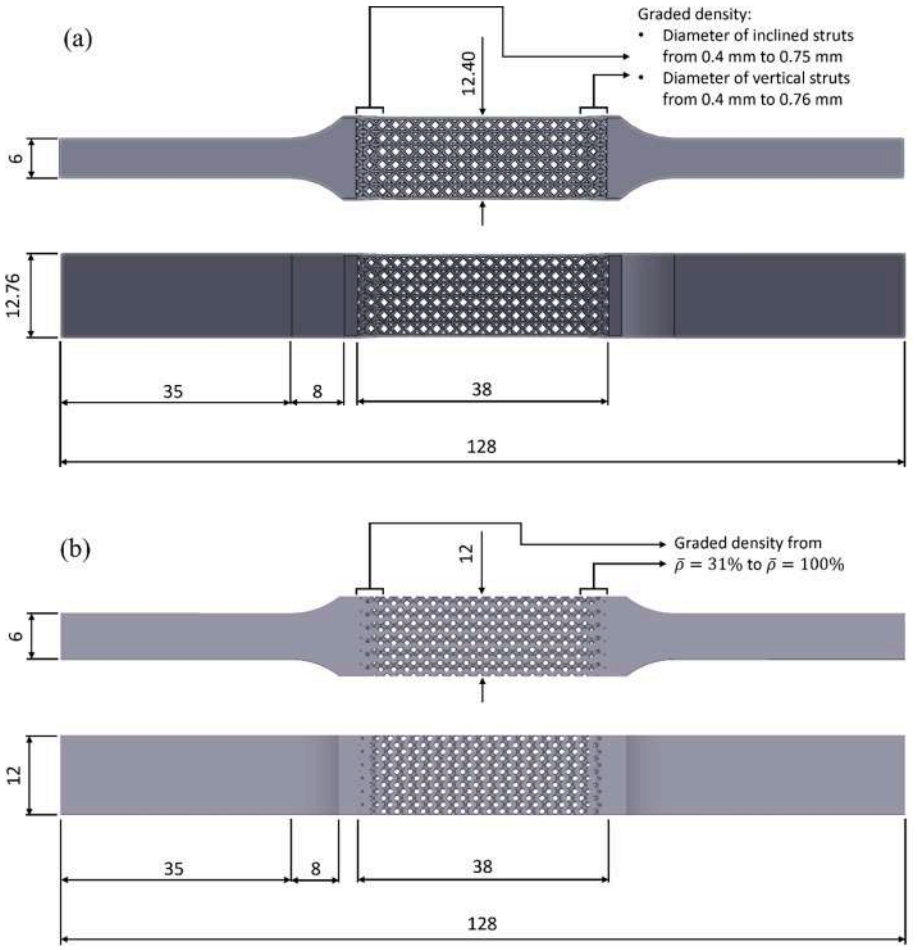

Fig. 2. Cellular specimen geometries: (a) FBCCZ and (b) gyroid (dimensions in mm).

with constant relative density is 12.4 mm × 12.4 mm for the FBCCZ specimen and 12 mm × 12 mm for the gyroid specimen. The difference of 0.4 mm is because the struts of the FBCCZ were not truncated at the boundaries but were designed to be complete. The graded density areas of the FBCCZ specimen were obtained by increasing the vertical struts from 0.4 mm to 0.76 mm and the inclined struts from 0.4 mm to 0.75 mm. This design choice explains the difference of 0.76 mm between the width of the grip portion of the FBCCZ and gyroid specimens. The base material of the cellular specimens is L-PBF 316L stainless steel. The bulk mechanical properties of this alloy were previously characterised through tensile and LCF tests on standard plain specimens [43,64].

2.2. Manufacturing process and metrological analysis

The cellular specimens were produced by L-PBF using a Concept Laser M2 Cusing machine. The processed AISI 316L steel powder had the chemical composition: 17.7 %Cr, 12.7 %Ni, 2.29 %Mo, 0.93 %Mn, 0.70 %Si, 0.02 %C. The particle diameters exhibited a Gaussian distribution ranging from 18.34 μm (10th percentile) to 45.00 μm (90th percentile), with a median value of 28.63 μm.

The STL files used to generate the input file for the printing phase were obtained with a slightly different path. The FBCCZ lattice specimen was modelled using a CAD system (SolidWorks), and then an STL of the geometry was exported. The gyroid cellular specimen was instead modelled using nTopology software, and the STL file was generated based on the implicit body of the geometry.

The samples were manufactured under an inert argon atmosphere with a residual oxygen level below 0.2 %. The adopted process parameters are reported in Table 1. The bulk area was exposed according to the island strategy described in [43]. Subsequently, a contouring scan was executed using optimised parameters to reduce process-related defects.

A stress-relieving heat treatment at 550 °C for 6 hours was performed before removing the specimens from the building platform. Finally, the grip section of the specimens was machined to guarantee perfect planarity of the faces and an optimal grip with the testing machine (Fig. 3 (a)).

The geometric and surface properties of the specimens were thoroughly examined according to the methodology specifically developed in [65] for AM structures. This analysis is crucial since the actual shape and surface conditions can significantly impact the specimens' mechanical behaviour.

A 7-axis Romer absolute arm equipped with a Hexagon RS5 laser scanner was utilised to inspect the geometric accuracy of the grip sections of the specimens. The measuring system error was within the interval ± 0.048 mm. The acquired point clouds were subsequently processed using the Hexagon PC-DMIS software and then aligned with the corresponding samples' CAD models, employing the best-fit method. Hence, the distance between the measured points and the CAD 3D model was calculated. The maximum deviation in the gripping areas was generally well within ± 0.1 mm, a value that ruled out the occurrence of unwanted bending stresses during testing.

The cellular portion of each specimen instead underwent inspection using a Sensofar S neox five axis 3D confocal microscope equipped with a Nikon EPI 20x objective. Multiple field-of-views were captured and stitched together with a 30 % overlap to obtain the entire surface of interest. The vertical resolution of the data acquisition was 1 μm. Each in-plane single scan was acquired with a resolution equal to 5 MP (megapixel), resulting in a 0.69 μm/px pixel size. The FBCCZ and gyroid overall geometrical conformity were evaluated by processing the acquired point clouds using PC-DMIS. Noise and unwanted tilting due to specimen misalignment were reduced to a minimum by appropriate filtering. Therefore, the reference 3D model and point clouds were aligned with the best-fit method. The same equipment was then used to assess the surface quality of the grip portions of the specimens. The acquired point clouds underwent cropping, filtering, and extraction of surface profiles from each sample. The length of all the extracted profiles was standardised to 25 mm. The data were then processed following the ISO 4287 standard to determine the average roughness (R_a) and average waviness (W_a), with a cut-off wavelength set at 2.5 mm.

Table 1
Laser-powder bed fusion (L-PBF) parameters for cellular specimens manufacturing.

	Laser power (W)	Scanning speed (mm/s)	Spot diameter (μm)	Hatch distance (μm)	Layer thickness (μm)
Bulk	180	600	120	105	25
Contour	150	350	70	–	25

2.3. Mechanical tests and fractographic analyses

The mechanical behaviour of the FBCCZ and gyroid specimens was first investigated through a quasi-static tensile test. The test started in strain-control mode with a strain rate equal to 6.66×10^{-5} s^{-1}, before switching to the displacement control with a higher speed of 1 mm/min. The static properties provided by the tensile tests were then used to determine the imposed strains in the LCF tests. A symmetric strain history with a constant amplitude was imposed during the fatigue tests, i.e., $R_\varepsilon = -1$. The strain amplitudes spanned from 0.3 % to 0.7 % for the FBCCZ structure, and from 0.3 % to 1.2 % for the gyroid. The frequency was adapted to achieve a strain rate of 4×10^{-3} s^{-1} for each test.

The static and cyclic tests were performed using an MTS 810 material testing machine with a built-in 100 kN load cell to measure the force. An MTS 634 axial extensometer was used to control the strain in a 25 mm gauge length. The experimental setup is depicted in Fig. 3 (b). The cyclic tests were stopped after the complete separation of the specimens except for the gyroid specimen tested at 0.3 % strain amplitude, which was stopped earlier and constituted the only exception. Nonetheless, the number of cycles to failure N_f was defined based on a 10 % stress drop from the linear softening that appeared during the cyclic test (see Fig. 4 (a)). This criterion is mentioned as the "parallel line method" from now on.

Results of the present work will refer to macroscopic stress and strain of the cellular specimens, as graphically defined in Fig. 4 (b). Precisely, the macroscopic stress is the ratio between the force F and the cross-section of the specimen A_0 (12 mm × 12 mm) regardless the presence of hollow regions, while the macroscopic strain is the ratio of the displacement measured by the extensometer ΔL divided by the gauge length L_0 (25 mm). The aim is to obtain a mechanical behaviour independent of the specimen geometry by considering the cellular structure as a homogeneous equivalent material. In that regard, the mechanical properties commonly defined for bulk materials in static and cyclic loading conditions (e.g. Young's modulus, yield strength, cyclic stress–strain curve) can be derived from the macroscopic stress–strain response.

Post-mortem fractographic analyses were conducted on cellular specimens to assess the global and local failure modes. In particular, macroscopic examination of the fractured specimens, which was performed by using a stereoscope, was followed by detailed microscopic analyses using a Zeiss Evo 40 Scanning Electron Microscope (SEM).

3. Results and discussion

3.1. Dimensional accuracy and surface roughness

The surface properties and the geometric accuracy of the FBCCZ and gyroid structures were analysed using the confocal optical microscope. The distance between the measured points and the reference surfaces of the cellular structures was calculated, obtaining the colour map of geometric errors, see Fig. 5 (a-b). The maximum deviation is generally within ± 0.1 mm. As expected, the major anomalies are predominantly

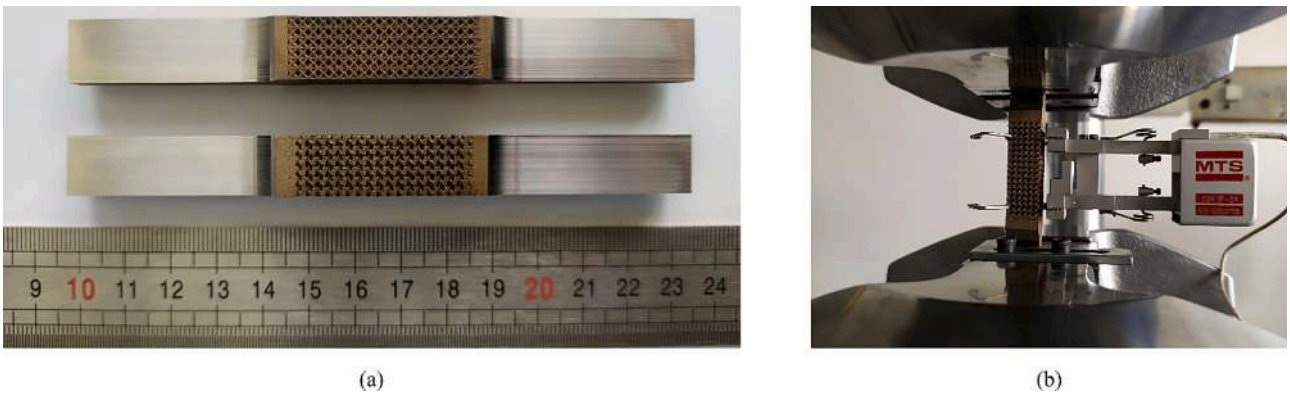

Fig. 3. (a) FBCCZ and gyroid specimens and (b) experimental setup for low cycle fatigue tests.

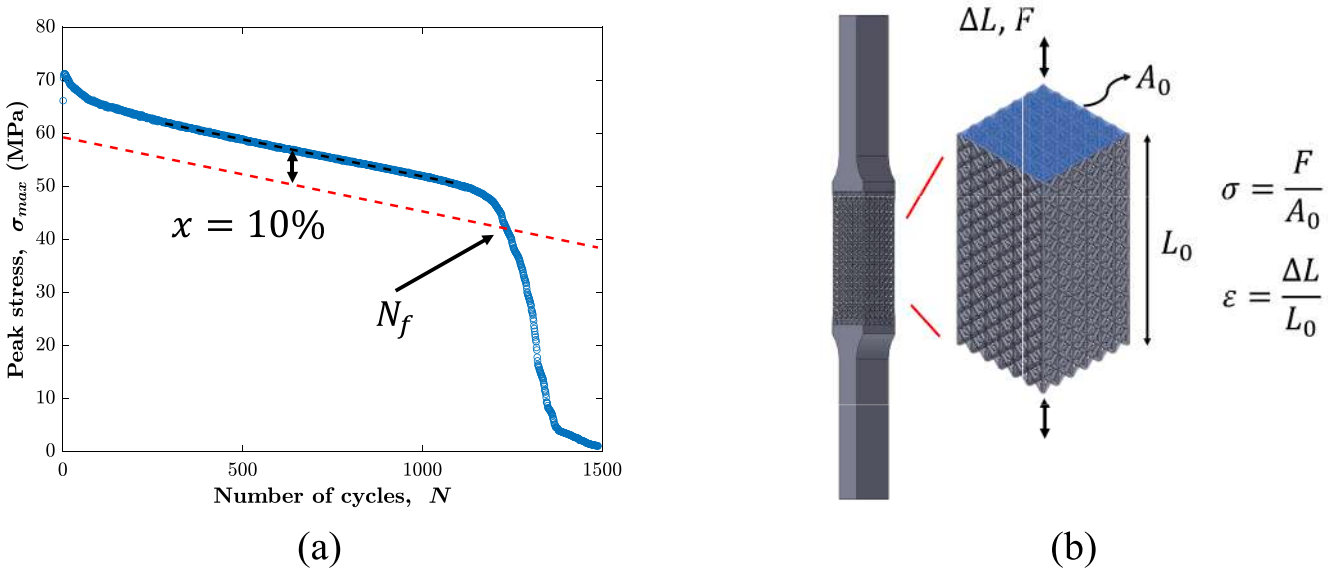

Fig. 4. Definition of the quantities in mechanical tests: (a) criterion for the determination of the number of cycles to failure and (b) definition of macroscopic stress and strain.

located in the proximity of down-facing surfaces, where inadequate heat removal is known to cause the formation of dross, or near small features (e.g. small holes of the graded density areas) [9,65]. The dimensional error is, therefore, well within the typical accuracy limits of L-PBF systems.

The diameter of the vertical and inclined struts of the FBCCZ lattice and the thickness of the vertical and horizontal walls of the gyroid were measured by processing the point cloud data. The measurements were repeated five times for each specimen, obtaining the boxplots shown in Fig. 5 (c). The upper and lower bound of the box refers to the 25th and 75th percentile, respectively. The middle line is instead the median of the data. The whiskers extend to the maximum and minimum values excluding the outliners, which are values further than 1.5 times the interquartile range from the up or bottom of the box. Each measurement is shown by means of a scatterplot, identifying each specimen with different colours. As expected, the vertical struts of the FBCCZ and vertical walls of the gyroid are accurately reproduced, with geometric errors never exceeding 60 μm for the former and 130 μm for the latter. However, as the angle relative to the build direction increases, such as in the case of inclined struts of the FBCCZ and horizontal walls of the gyroid, the geometric error also increases. Considering the horizontal walls of the gyroid, the error can exceed 300 μm, primarily due to significant dross formation resulting from poor thermal exchange.

Afterwards, the surface properties of the flat lateral surfaces in the clamping areas of the specimens were also analysed. The roughness average was 7.48 μm, and the waviness average was 2.67 μm. The standard deviations of the roughness and waviness measurements were 0.65 and 0.72 μm, respectively, indicating good process repeatability.

3.2. *Quasi-static tensile tests*

Stress–strain curves of the FBCCZ and gyroid cellular materials derived from the tensile tests are shown in Fig. 6. A quantitative analysis of the curves gives the static properties listed in Table 2. The mechanical properties of the base material - produced by the authors in a previous study - are also reported for a direct comparison [64]. The difference in elongation between the FBCCZ and gyroid specimens is clear from a glance at the overall curves. The elongation at fracture (A%) of the gyroid specimen is nearly ten times higher than the FBCCZ specimen. Zooming in the first part of the curve, as shown in the inset of Fig. 6, the higher stiffness of the FBCCZ compared to the gyroid cellular specimen becomes evident. The estimated Young's modulus (E) of the FBCCZ is about two times the one of the gyroid. It is also apparent that the gyroid cellular material has a yield strength at 0.2 % of plastic strain ($\sigma_{y,0.2\%}$) definitively lower than the FBCCZ. However, there is a moderate difference of only 20 MPa in the ultimate tensile strength (σ_{UTS}) recorded

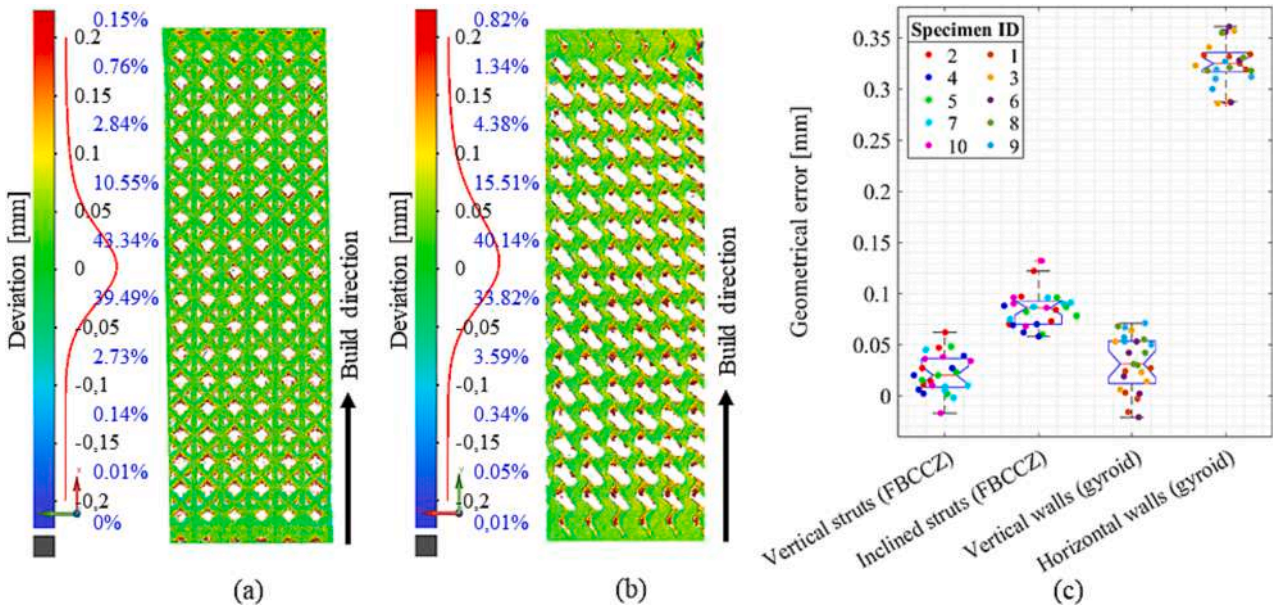

Fig. 5. Deviation between the as-built and nominal surfaces of (a) FBCCZ and (b) gyroid cellular structures; (c) geometrical error quantification on vertical and inclined struts for the FBCCZ specimens and on vertical and horizontal walls for the gyroid specimens.

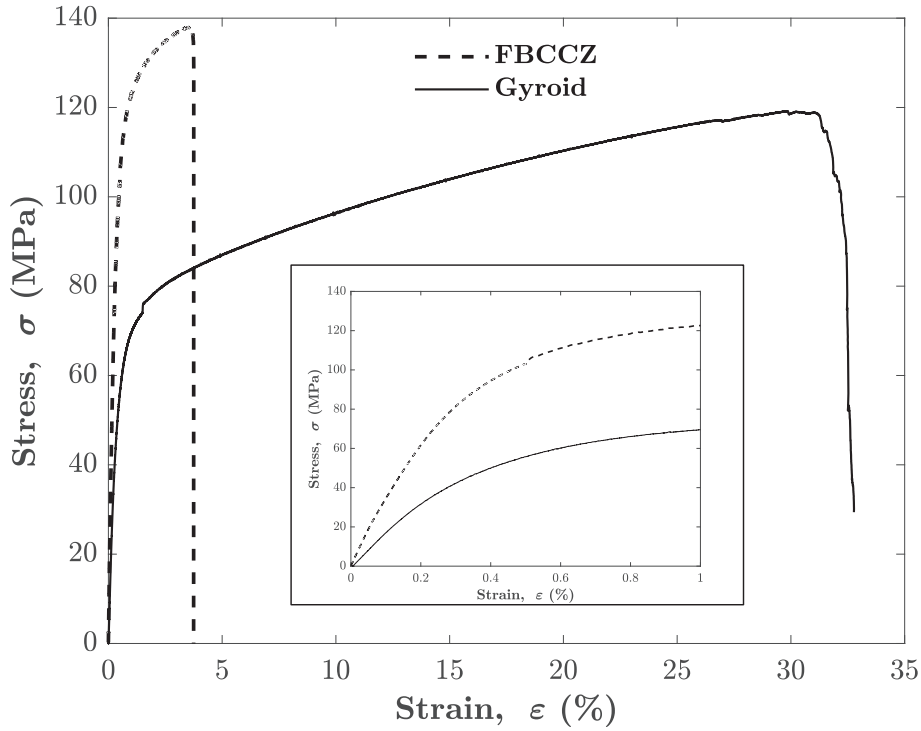

Fig. 6. Stress–strain curves of the FBCCZ and gyroid cellular materials obtained from the quasi-static tensile test. A magnification of the low-strain regime is shown in the inset.

Table 2
Relative density and quasi-static tensile properties of the base material (L-PBF 316L steel), FBCCZ and gyroid cellular materials.

	$\overline{\rho}$	E(MPa)	$\sigma_{y.0.2\%}$(MPa)	σ_{UTS}(MPa)	A%
L-PBF 316L steel [64]	100 %	198,562	527	660	32.7 %
FBCCZ	31 %	37,216	101	138	3.75 %
Gyroid	31 %	17,954	57	119	32.8 %

during the tests. The properties of the base material and the geometry of the gyroid structure can give a possible explanation for this behaviour. In fact, the high ductility of the L-PBF 316 steel allows for a change in the mechanical response of the gyroid, from bending-dominated to partially stretching-dominated, thanks to the rotation of the "pseudo-struts" along the loading direction [52]. On the contrary, the vertical struts in the FBCCZ cell make the response stretching-dominated from the beginning of the test, which is reflected in the high stiffness, preventing taking full advantage of the reorientation of the inclined struts. Furthermore, in the FBCCZ cell, the high ductility of the base material is

not entirely exploited due to the presence of sharp notches at nodes that explain the low elongation of this type of cell.

A side view of FBCCZ and gyroid specimens after tensile tests is reported in Fig. 7 (a,c). The FBCCZ specimen exhibits a failure with a small amount of deformation located near the fractured region between two rows of cells. This position is the weakest in the FBCCZ structure due to the strong inhomogeneity of stress distribution with high concentration in the nodes. The gyroid, on the contrary, is characterised by a diffuse necking along the gauge length, thanks to the more homogeneous stress distribution. Fig. 7 (b) displays a representative fracture surface of the FBCCZ structure, where the growth and coalescence of voids are evident. The nucleation of the voids was likely triggered by the defects already present in the material, which could further reduce the ductility of the FBCCZ cellular material. The fracture surfaces of the gyroid specimen are instead characterised by a less irregular surface, as reported in Fig. 7 (d).

3.3. Cyclic stress response

The change in stress amplitudes up to the number of cycles to failure during strain cycling is reported in Fig. 8 (a-b) for both FBCCZ and gyroid cellular materials. In this figure, the cyclic response for both the tested materials is shown using two different approaches. Fig. 8 (a) has the number of cycles in the logarithmic scale on the *x*-axis, whereas Fig. 8 (b) reports the life fraction (the number of cycles divided by the number of cycles to failure) in a linear scale. The criterion to determine the number of cycles to failure was explained in Section 2.3. An exception is the gyroid specimen tested at 0.3 % strain amplitude, which was stopped before complete specimen separation. Furthermore, that specimen did not show any clear drop of maximum stress during the test – the stress was already below 10 MPa after 47,000 cycles. Owing to these reasons, the number of cycles to failure for this specific test was established at the cycle at which the maximum stress decreased by 40 % from the overall maximum stress recorded during the test. A value of 40 % was chosen because it corresponds to the average value of the stress drop at the number of cycles to failure defined with the "parallel line method" for the other tested gyroid specimens. Therefore, the two criteria are rather consistent. The number of cycles to failure for each low cycle fatigue test are reported in Table 3.

The FBCCZ structure clearly withstands higher stresses than the gyroid one for all the tested strain amplitudes. Nevertheless, both the unit cell topologies share some common features during the cyclic response. The stress amplitude increases for about five cycles at the beginning of the test, which is consistent with the behaviour of the base material [43]. However, the majority of the life of the specimens is covered by a linear cyclic softening, which starts immediately after the fast hardening for the FBCCZ cell and a short non-linear softening for the gyroid cell. The onset of the linear softening is located between 10 and 30 % of the life fraction, whereas the end is at approximately 90 %. A non-linear drop of the stress associated with the propagation of a macrocrack can be recognised in the last part of the specimen life. In Fig. 8 (b), the slope of the linear softening part is nearly constant, independent of the strain amplitude values. However, it must be noted that this plot depicts the stress amplitude against the life fraction, not the number of cycles. Therefore, the slope of the stress amplitude against the number of cycles changes with the strain amplitude, but it becomes almost constant if multiplied by the number of cycles to failure: $(\mathrm{d}\sigma_a/\mathrm{d}N)N_f \cong \text{costant}$. In other terms, the smaller the number of cycles to failure (or the higher the strain amplitude), the steeper the linear softening.

As a final remark, all the tested specimens did not reach any stabilised condition in cyclic loading. The stabilised condition refers to a stress amplitude, and hence a stress–strain hysteresis loop, that remains unchanged during cycling, and it is usually attained after a certain number of cycles, depending on the material. This behaviour is

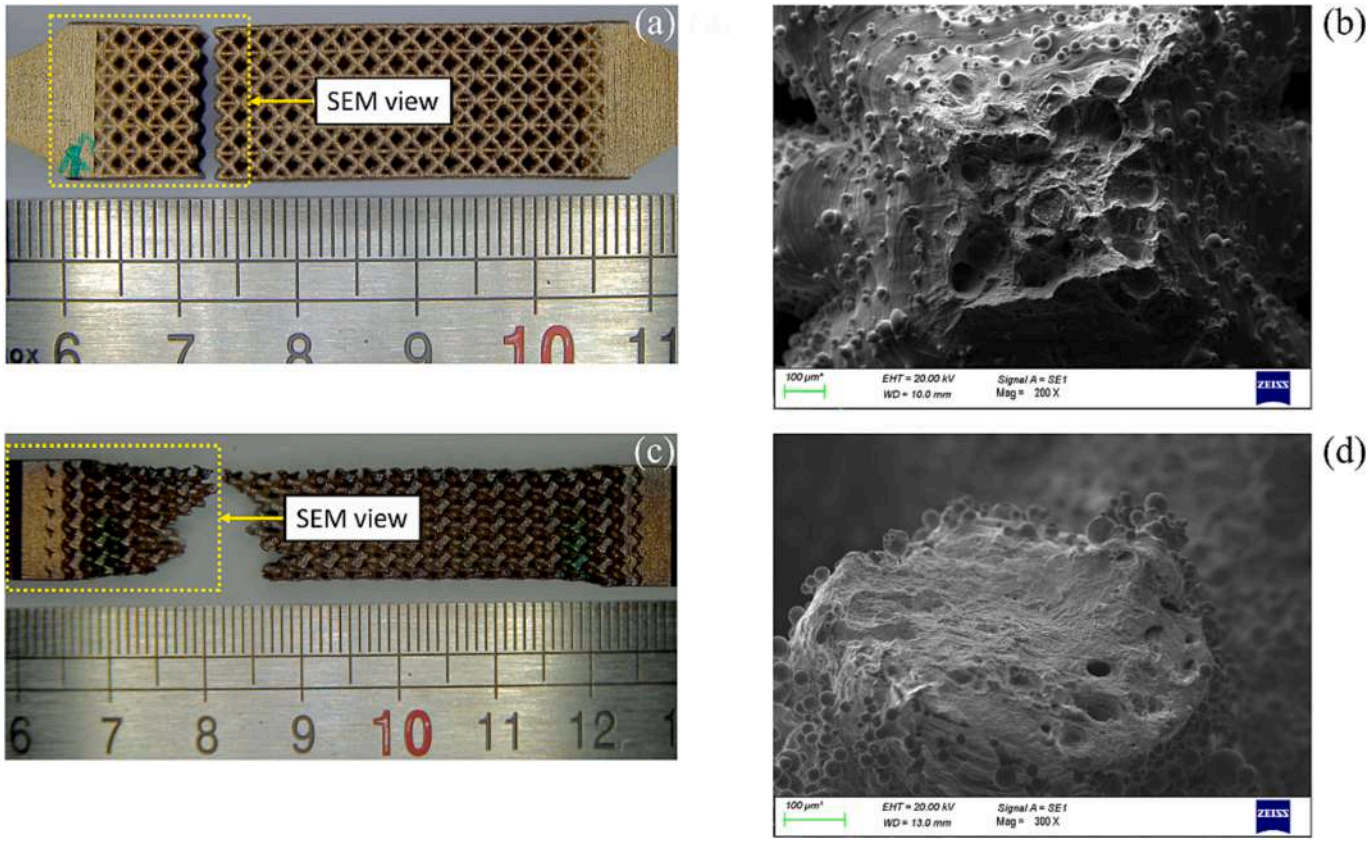

Fig. 7. Quasi-static failures and fracture surfaces: (a) side view of the broken FBCCZ specimen and (b) fracture surface of an internal node revealing void growth and coalescence; (c) side view of the broken gyroid specimen and (d) fracture surface of a "pseudo-strut" showing a relatively flat surface.

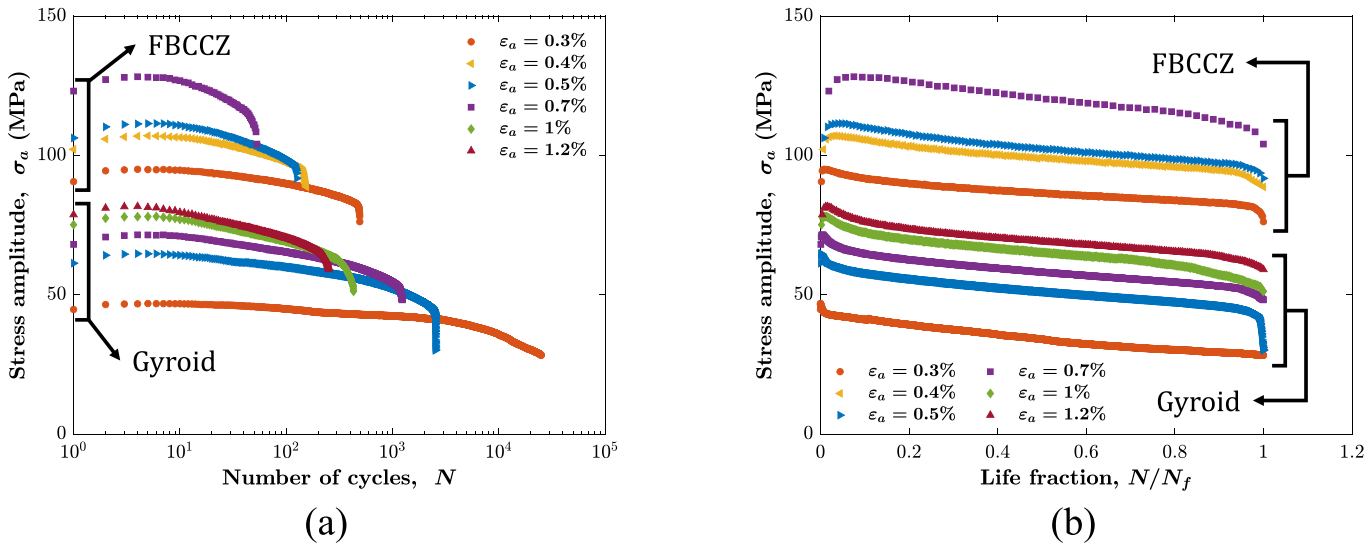

Fig. 8. Cyclic stress response of FBCCZ and gyroid cellular materials: stress amplitude versus (a) number of cycles in logarithmic scale and (b) life fraction in linear scale.

Table 3
Results of the low cycle fatigue tests for FBCCZ and gyroid cellular materials: number of cycles to failure, stress and plastic strain amplitudes (referred to the half-life cycles).

	ε_a(%)	N_f	σ_a(MPa)	$\varepsilon_{pl,a}$
FBCCZ	0.3	492	87	0.000657
	0.4	155	99	0.001258
	0.5	126	103	0.001899
	0.7	53	120	0.003374
Gyroid	0.3	25,057	35	0.000604
	0.5	2531	51	0.001748
	0.7	1234	58	0.003049
	1	430	66	0.005862
	1.2	251	70	0.007455

somehow predictable since even the base material did not present a complete stabilisation too. Moreover, given that the plastic strain field in cellular structures is highly inhomogeneous, only a few regions can indeed accumulate enough plastic strain to reach a quasi-stabilised condition before specimen failure, while the overall macroscopic response cannot.

3.3.1. *Cyclic material softening and fatigue damage*

The cyclic response of the FBCCZ and gyroid cellular materials was investigated more in-depth by looking at the change in maximum and minimum stress with the number of cycles and, therefore, in the mean and amplitude stress. The responses of the FBCCZ and gyroid specimens tested at 0.3 % and 0.7 % strain amplitudes, respectively, are presented in Fig. 9 (a-b). These two tests were selected for the comparison because the cyclic stress responses versus the life fraction are similar (i.e. beginning and end of the linear softening are approximatively at 25 % and 90 % of the life fraction), and the number of cycles of failure are comparable too. The maximum stress decreases faster than the (absolute) minimum stress during the linear softening phase. This trend leads to the development of negative mean stresses. This type of cyclic behaviour was found for each tested specimen. However, the linear softening for the FBCCZ cellular material begins earlier in the test and with a different slope for the maximum and minimum stress values. In contrast, the cyclic softening of the maximum and minimum stress for the gyroid specimens maintains a similar trend for a higher number of cycles.

Unfortunately, other literature studies on cellular structures, or

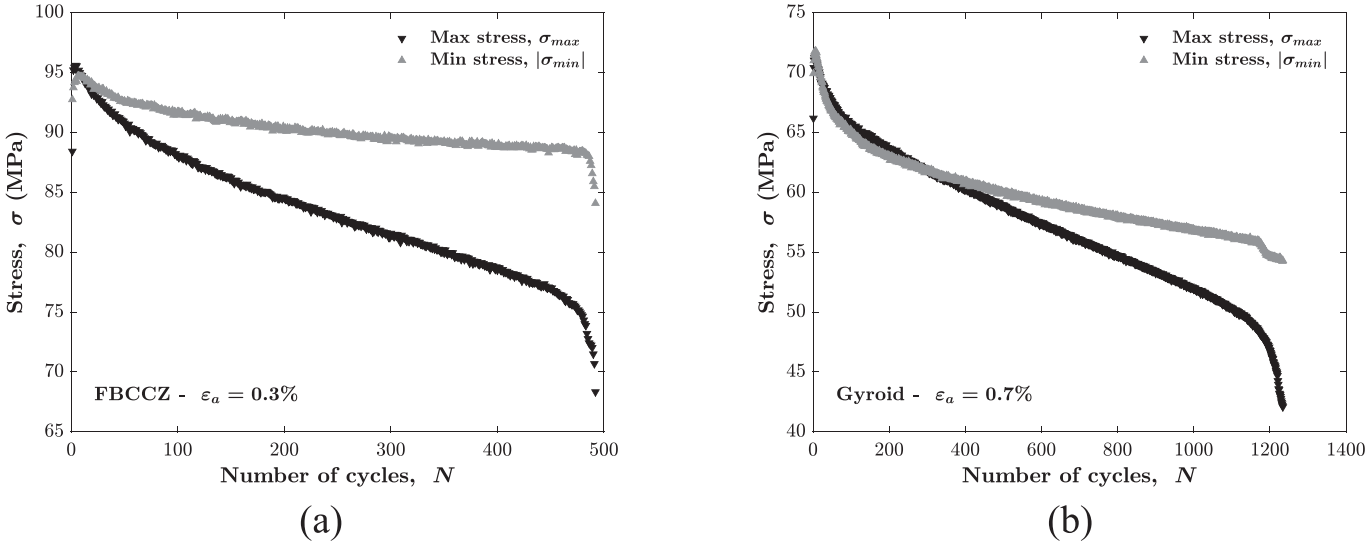

Fig. 9. Maximum and minimum stress versus the number of cycles: (a) FBCCZ specimen tested at a strain amplitude of 0.3% and (b) gyroid specimen tested at a strain amplitude of 0.7 %.

metal foams, report fatigue tests under load control, so a direct comparison with existing literature results is not viable. Nonetheless, many studies can suggest insights into the cyclic response in strain control loading. From an historical perspective, metal foams have been investigated earlier than cellular structures. As an example, relevant studies by Ashby et al. described the failure modes of metal foams under fatigue loading in tension–tension and compression-compression [66]. Under tension–tension loads, an initial ratcheting phase, with an increasing mean strain, progresses during the test until it reaches a strain value that leads to a rapid specimen elongation. On the other hand, during compression-compression, the strain accumulates at a gradually decreasing rate in the first stage. Then, it keeps growing at a reduced ratcheting rate until it reaches the final stage, where the strain grows faster with one or more jumps depending on the type of metal foam. In the final stage, the elastic modulus during unloading decreases, as reported by different authors [67,68]. In both loading cases, the gradual accumulation of mean strain per cycle is associated with a combination of cracking and ratcheting, though the tests were conducted in the macroscopic elastic range. On the contrary, the final stage is related to the densification of the foams in compression-compression and the propagation of a macrocrack in tension–tension. Failure modes similar to that of metal foams under fatigue loading were then found in cellular structures by many authors [28,68,69]. In compression-compression, an initial phase has been identified with an increasing mean strain at a slow rate. An evident increase in strain amplitude, which is related to the early damage of a strut, can be recognised after a certain number of cycles. At the same time, the mean strain grows faster and faster until it reaches a high rate. In that way, the beginning of the second stage is usually related to the number of cycles to damage initiation, whereas the third stage is the number of cycles to failure. The same notions were also extended to tension–tension and tension–compression loading conditions [35].

The above discussion allows the cyclic stress response in Fig. 9 (a-b) to be reinterpreted. The asymmetric behaviour between maxima and minima of the stress can be likely due to some micro-damage processes at the level of single struts that decrease the cellular structure stiffness in tension faster than in compression. The opposite behaviour happens in load control tests, where the mean strain increases. On the other hand, the cyclic softening in compression is likely to be mainly related to the cyclic softening of the material and only partially to the damage. When cellular specimens are loaded in an elastoplastic regime, it is indeed challenging to separate the softening due to plastic deformations from that caused by damage degradation. Nonetheless, the minimum stress in compression presented a cyclic softening like the one reported for the base material [43].

The elastic moduli in tension, E_t, and compression, E_c, were estimated for each recorded stress–strain hysteresis loop to gain further insights. In particular, the elastic moduli in tension and compression were obtained in the unloading phase from the maximum and minimum stress, respectively. In Fig. 10 (a-b), the elastic moduli values are plotted against the number of cycles for a test of each type of cellular structure. The mean stress at each cycle is also depicted in the same plot. It can be noticed that the elastic modulus in compression remains almost stable during the tests. On the contrary, the elastic modulus in tension starts to decrease with a linear trend similar to that of the mean stress. Therefore, the different slopes in the linear cyclic softening between the stress maxima and minima, and hence the development of negative mean stress, seem correlated to a stiffness degradation of the cellular structures in tension.

From the above consideration, the cycle at which the mean stress starts to decrease linearly to negative values can be interpreted as the onset of damage in strain control loading. The damage process begins early in the test in this respect and influences the macroscopic response of the cellular structures. The moment when the mean and amplitude stress of the cycles begin to drop faster can be instead associated with the formation and subsequent propagation of a macrocrack. The final macrocrack propagation stage is characterised by a fast decrease of the stresses alternated by discontinuities in the rate but without a sudden separation of the specimen. In fact, the progressive failure of the cells leads to discontinuous crack propagation in the lattice [36].

3.4. Stress–strain hysteresis loops and cyclic curve

Some of the recorded stress–strain hysteresis loops are displayed in Fig. 11 (a-b) for both cellular materials when loaded at a strain amplitude of 0.7 %. The cyclic softening behaviour is evident by looking at the decrease of stress maxima and minima. Furthermore, the hysteresis loops change in shape during cycling, and, at the same time, they shift to negative mean stresses. In the last cycles, the elastic modulus in tension is lower than in compression. The compressive branch is also distinguished by an inflection point. For bulk metallic plain specimens, this peculiar shape of the hysteresis loops is related to the closure and opening of a macrocrack in the specimen [70], analogously to what observed in fatigue crack opening displacement [71].

Furthermore, in analogy with conventional bulk metals, stabilised stress–strain hysteresis loops can be analysed to draw a cyclic strain-life curve for both the FBCCZ and gyroid cellular materials. The stabilised hysteresis loops are obtained when the material reaches cyclic stabili-

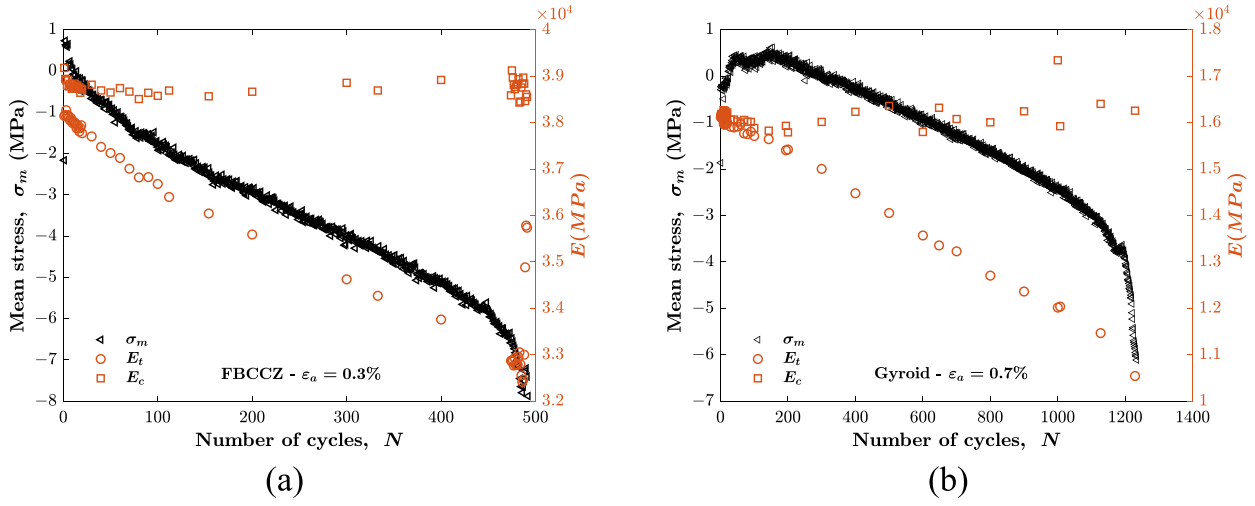

Fig. 10. Mean stress and elastic moduli in tension and compression versus the number of cycles: (a) FBCCZ and (b) gyroid specimen tested at a strain amplitude of 0.3% and 0.7%, respectively.

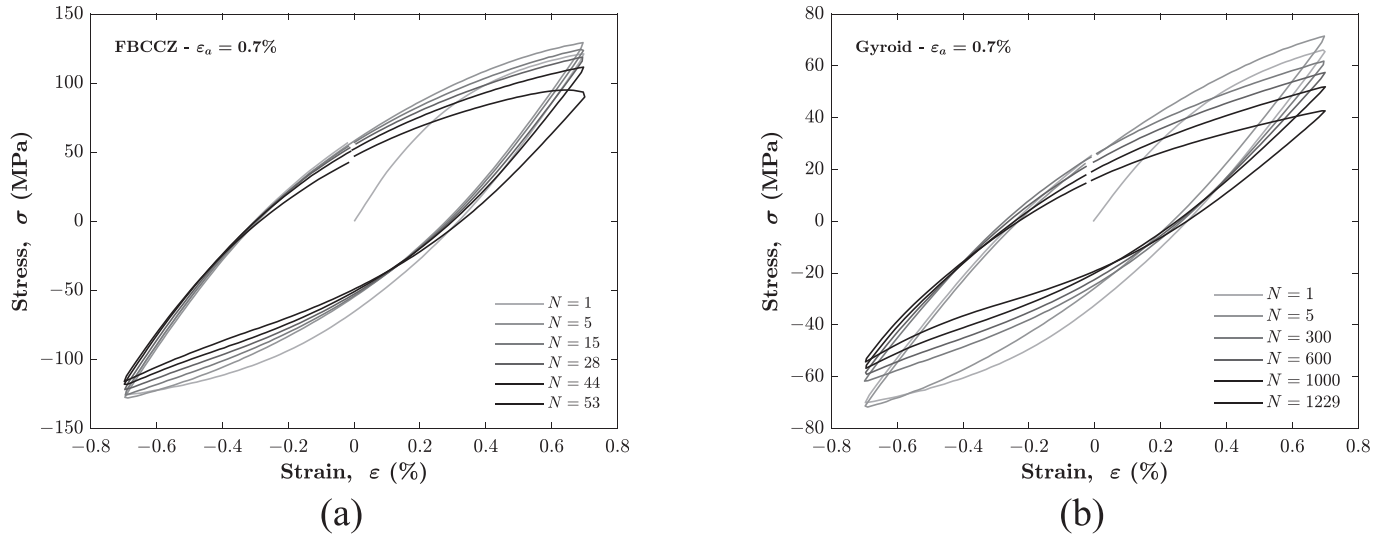

Fig. 11. Stress–strain hysteresis loops of the test at 0.7% strain amplitude: (a) FBCCZ and (b) gyroid cellular materials.

sation, and they are used to describe the material constitutive behaviour in strain cycling conditions, which is different from the monotonic loading case. A stabilised hysteresis loop would be therefore required for obtaining the stress amplitude and, consequently, the plastic strain amplitude related to the imposed strain amplitude during cyclic loads. However, the linear cyclic softening, mentioned in the previous Section 3.3, hides any sign of cyclic stabilisation. Therefore, the hysteresis loops at half-life are considered representative of the average cyclic response of the cellular materials though they are already characterised by a lower elastic modulus in tension than in compression. This is a standard procedure, and it has been reported by distinguished researchers [72,73]. Fig. 12 (a) depicts the half-life stress–strain hysteresis loops for the FBCCZ and gyroid specimens for every strain amplitude, whereas Fig. 12 (b) compares the monotonic and cyclic curves. The markers represent the pairs of stress amplitudes σ_a at half-life and plastic strain amplitudes $\varepsilon_{pl,a}$ listed in Table 3. The cyclic curve of the FBCCZ lattice material essentially overlaps the monotonic one, suggesting that the cyclic softening is negligible. On the contrary, the gyroid cellular material presents an apparent softening that leads to a cyclic curve lower than the monotonic curve.

The cyclic curves were fitted with the widely-employed Ramberg-Osgood type equation:

$$\varepsilon_a = \frac{\sigma_a}{E} + \left(\frac{\sigma_a}{K'}\right)^{1/n'} \tag{3}$$

where K' and n' are the cyclic strength coefficient and cyclic strain hardening exponent, respectively; their values resulting from a best-fitting are reported in the last two columns of Table 4.

Table 4
Parameters of the Manson-Coffin strain-life curve and Ramberg-Osgood cyclic curve for FBCCZ and gyroid cellular materials.

	σ_f'/E	b	ε_f'	c	K'(MPa)	n'
L-PBF 316L steel	0.005242	−0.0845	0.66849	−0.5965	822	0.0973
FBCCZ	0.009449	−0.2061	0.116976	−0.7616	281	0.1552
Gyroid	0.011228	−0.1428	0.245694	−0.5624	291	0.2840

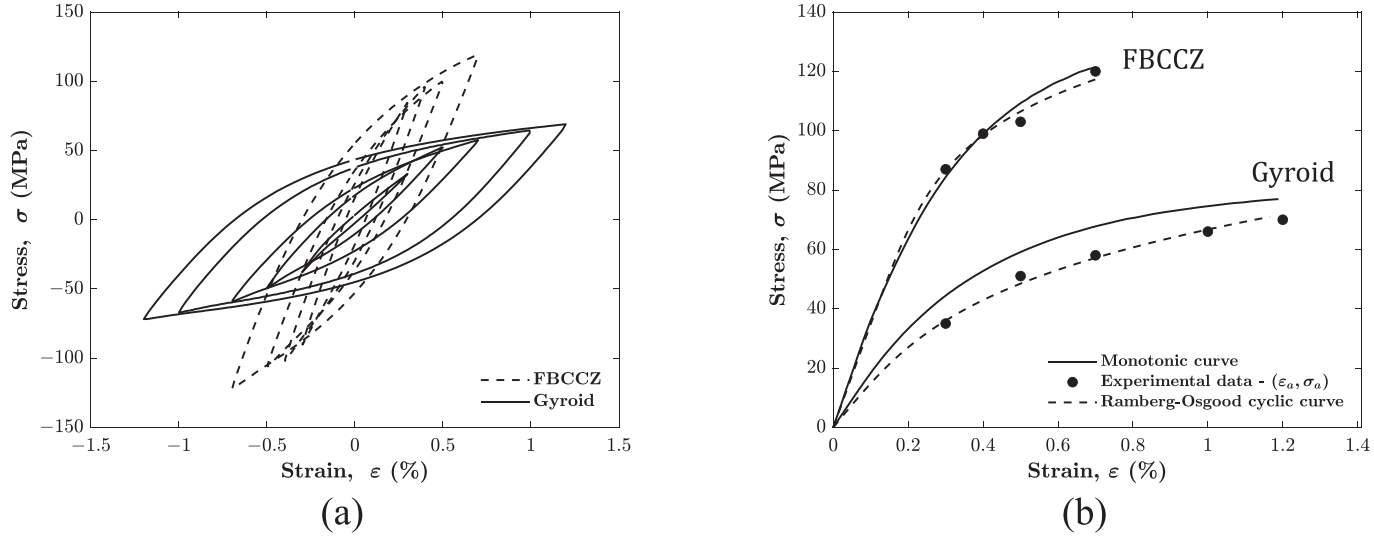

Fig. 12. Cyclic stress–strain response: (a) half-life hysteresis loops for FBCCZ and gyroid cellular materials at different strain amplitudes; (b) monotonic and cyclic curves for both the FBCCZ and gyroid cellular materials.

3.5. Strain-life curve

The numbers of cycles to failure at each strain amplitude are depicted in Fig. 13 (a) as markers (black solid triangles for the FBCCZ cellular material, black solid circles for the gyroid). The elastic (blue down-pointing empty triangles for FBCCZ, blue empty triangles for gyroid) and plastic strain amplitudes (red empty diamonds for FBCCZ, red empty squares for gyroid) for each test are also illustrated in the same figure. The experimental data were fitted by a Manson-Coffin model, as usually done for bulk materials:

$$\varepsilon_a = \frac{\sigma_f'}{E}(2N_f)^b + \varepsilon_f'(2N_f)^c \tag{4}$$

where the fatigue strength coefficient σ_f' and exponent b are the fitting parameters of the elastic part, whereas the fatigue ductility ε_f' and exponent c are the parameters of the plastic part.

The Manson-Coffin curves are reported in Fig. 13 (a), together with the straight lines related to the elastic and plastic parts, which were fitted separately to obtain the model parameters. The least-square fitting procedure was used [72]. The elastic and plastic straight lines for the FBCCZ lattice material are visually shifted to the left with respect to the ones of the gyroid. However, the Manson-Coffin parameters listed in Table 4 reveal that also the fatigue strength and ductility exponents, b and c, are slightly different among the unit cell topologies.

In Fig. 13 (b), the strain-life curves of the FBCCZ and gyroid cellular materials are compared to the curve of the base (bulk) material. Despite the low number of tests, an apparent different behaviour is obtained between the two cellular materials, enforced by a relatively low scatter that allows some remarks to be confidently made. At any strain amplitude, FBCCZ specimens have fatigue lives that are between 25 and 100 times shorter than 316L steel bulk specimens. Gyroid specimens, on the contrary, have shorter fatigue lives than the base material at high strain amplitudes, but more similar when approaching a low strain amplitude of 0.3 %. It is important to remind that these tests are carried out controlling the macroscopic strain, therefore results must be carefully interpreted when considering a fatigue regime close to the HCF, in which stresses can become the driver of the fatigue phenomenon. Indeed, the similar fatigue life of gyroid vs. bulk material at low strain amplitudes can possibly be explained by noting that the gyroid cellular structure is less stiff than the bulk material due to its greater porosity, leading to a lower macroscopic stress of the former when subjected to the same macroscopic strain. Yet, it is equally true that the local stress field in the gyroid specimens is rather inhomogeneous, with zones characterised by high stress magnitudes. These highly stressed zones, however, are expected to be small enough to counterbalance the global stress attenuation effect due to the more compliant behaviour. The same arguments can be made as far as the FBCCZ cell is concerned, except that the presence of significantly sharper notches, and the consequent increase of local stresses, negatively impact the fatigue life. Different outcomes would be obtained in the case of load-controlled tests and HCF stress-life curves. Indeed, cellular materials cannot attain fatigue strengths as high as the companion bulk material when subjected to the same macroscopic stress amplitude [33,74].

Similar comments on the comparison between the strain-life curves can be made by observing the Manson-Coffin parameters reported in Table 4. A general trend can be noticed in the fatigue ductility coefficient ε_f', which is the highest for the base material and the lowest for the less ductile FBCCZ lattice. The same holds for the fatigue strength coefficient. In fact, if the ratio σ_f'/E is multiplied by the Young's modulus of the considered type of specimen, the highest σ_f' is again for the base material and the lowest for the weak gyroid cellular material. As mentioned before, the exponents also change among the different specimens, but with a less explicable trend. A more reliable characterisation of the fatigue curves of these materials would require further tests for design purposes. In any case, the present paper aims at comparing the fatigue behaviour of the two analysed cellular materials, therefore, the presented experimental tests are sufficient to robustly draw significant conclusions.

3.6. Fatigue failures and fracture surfaces

The fracture surfaces of all the FBCCZ specimens are planar, as in the case of the specimen tested at a strain amplitude of 0.3 % and reported in Fig. 14 (a-b), and are situated in almost the same position along the gauge length. In particular, the specimens tested at 0.3 % and 0.4 % strain amplitudes failed between the 3rd and 4th cell rows, whereas the specimens tested at 0.5 % and 0.7 % failed between the 6th and 7th rows and 4th and 5th rows, respectively. The failure is always located at the nodes where there are 18 struts connected. This position is the weakest point in the structure for different reasons. First, these nodes have a high stiffness because of the contribution of a large number of struts, which leads to a gradual increase of stress and strain towards the node. This

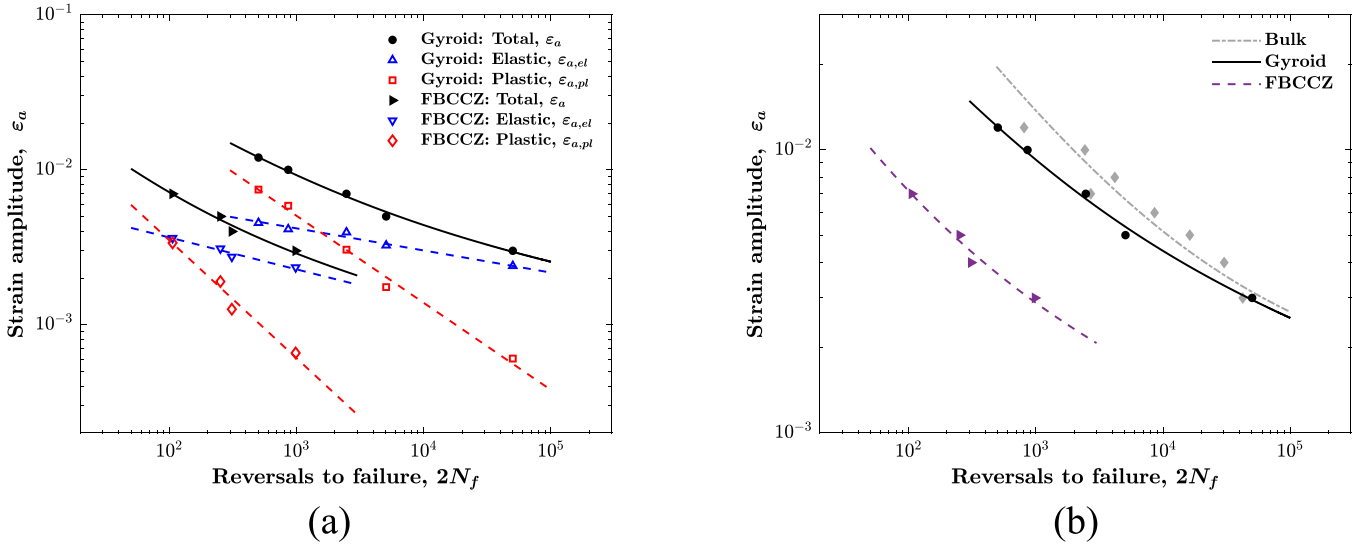

Fig. 13. Strain-life fatigue curves: (a) total, elastic and plastic strain amplitude versus number of reversals to failure for FBCCZ and gyroid cellular materials; (b) total strain amplitude versus number of reversals to failure for base material (L-PBF AISI 316L steel), FBCCZ and gyroid materials.

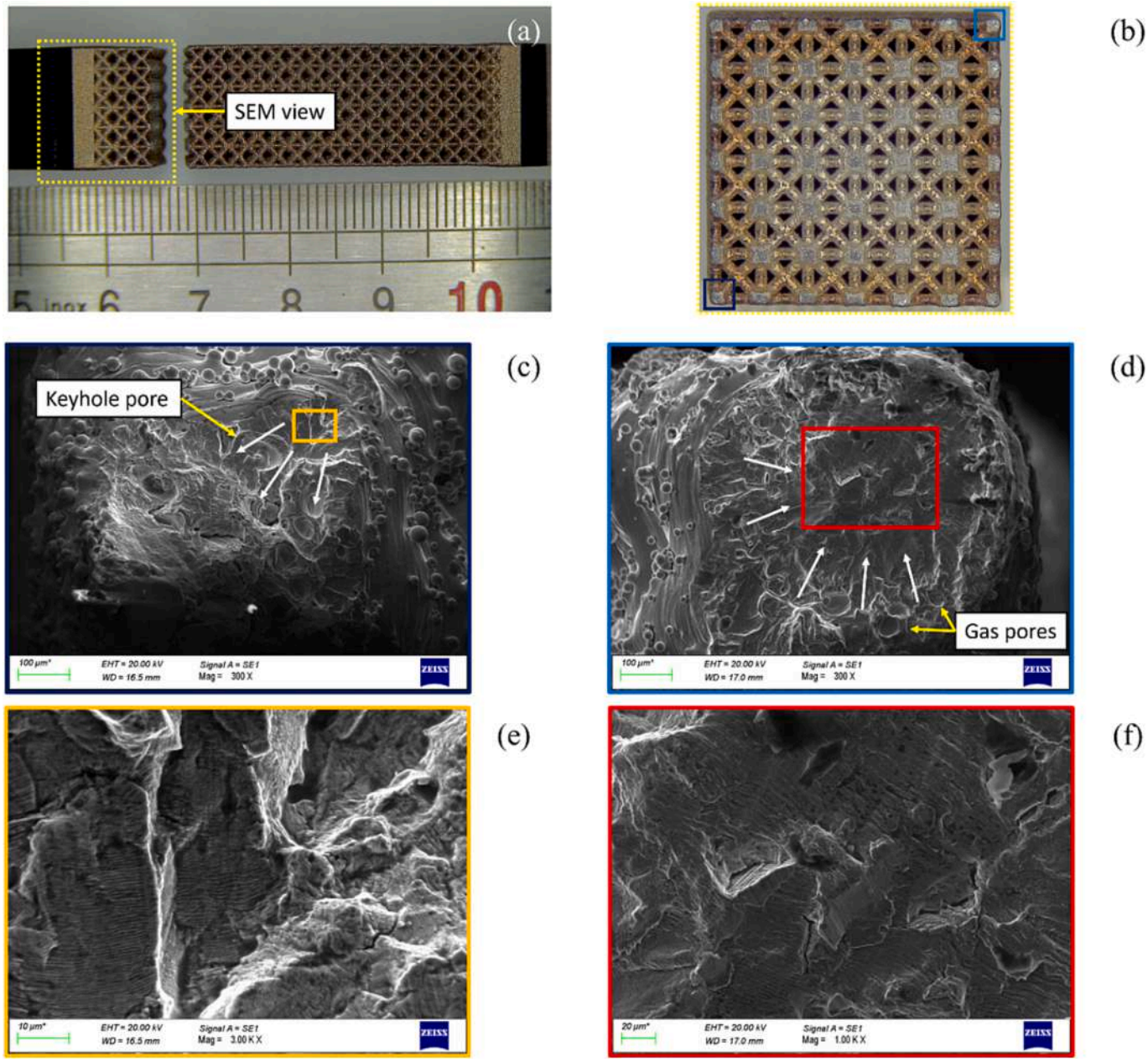

Fig. 14. Fractographic analysis of the FBCCZ specimen tested at 0.3 % strain amplitude: (a) side view of the broken specimen and (b) macroscopic top view of the fracture surface; (c) fracture surface at lower left corner node revealing ductile and fatigue damage characterised by multiple crack nucleation and (e) fatigue striations; (d) fracture surface at upper right corner node failed completely by fatigue damage as highlighted by the flat surface in presence of (f) fatigue striations with large spacing.

behaviour is, to some extent, similar to that of a plate with welded stiffeners that lead to a structural stress concentration. Second, the plane passing through the nodes is the one with the smallest load-bearing section area. Third, the small opening angle between the inclined struts connected to the node determines a sharp notch that further increases the stress and strain locally. In fact, also other studies on a slightly different unit cell geometry, namely FCCZ, reported the nodes as the fatigue fracture position in the lattice structure [31,75]. Last but not least, internal porosity can also contribute to a further weakening of the material inside the lattice nodes [76].

Microscopic analysis with SEM revealed that some of the nodes failed by fatigue damage, whereas others by quasi-static ductile fracture. For example, in Fig. 14(c), cracks nucleated and propagated through the node until a quasi-static failure occurred, whereas the node analysed in Fig. 14(d) is entirely flat; the flatness is driven by the smaller cross sectional area that the crack prefers to follow during its propagation. Multiple crack initiations and ratchet marks are visible in both nodes of Fig. 14(c, d). The nucleation of cracks in different positions is typical of high loads but can also be further promoted by zones with stress concentrations. At higher magnification, fatigue striations are visible (Fig. 14(e, f)). Some gas or keyhole pores are present in the fracture surfaces. The same amount of defects was also found in the internal nodes of the specimen. A few cracks nucleated from the pore can be noticed in Fig. 14(c), but they do not seem to be the leading cracks. Overall, it can be stated that internal defects and also surface roughness play a minor role in low cycle fatigue. At least, the main driver in locating the fatigue fracture position is the nominal geometry of the cellular structure. In any case, it appears that defects and surface roughness also contributed to the decrease in the total fatigue life of the FBCCZ cellular structures in the studied regime. In fact, the reported

defects can offer a favourable path for fatigue crack propagation.

Fracture surfaces of the FBCCZ specimen tested at the higher strain amplitude of 0.7 % are characterised by a similar morphology to the one tested at 0.3 %. Fig. 15(a) depicts the fracture surface on a node on the inside of the specimen. Crack nucleation sites are visible all around the free surface, internal porosity and unmelted powders. On the contrary, the corner node reported in Fig. 15(b) reveals an irregular morphology ascribable to a partially ductile failure. Unfused powder particles within some of the internal pores can be noticed on the fracture surface.

A clear difference in the amount of the regions characterised by fatigue and ductile damage is not visible at different strain levels. This evidence might be explained by considering that all the specimens failed gradually without a sudden separation, leading to a failure dominated by fatigue damage. A further explanation could be that all the tested strain levels are high enough to result in the same failure mechanism. In fact, also the specimen tested at a strain amplitude of 0.3 % failed at a rather low number of cycles ($N_f = 492$).

Differently from FBCCZ, the fracture surfaces of gyroid specimens extend in multiple planes. The gyroid specimen tested at 0.5 % strain amplitude is examined in Fig. 16(a, b). In the gyroid cell, nodes are not as easy to be identified as in FBCCZ; moreover, different gyroid cells failed at distinct locations. Nevertheless, the majority of cells failed in the same most stressed region due to the combination of bending and tensile loadings. Actually, as discussed by Yang et al., a small torsional load is also present at the same position [29]. In Fig. 16(c), a fracture dominated by fatigue damage is evident, whereas no signs of ductile fracture are visible. Fatigue striations can be noticed in Fig. 16(e) in the middle of the surface. Similar fracture morphologies were observed for most of the cells and only a few failed by ductile damage. One of the cells that failed by static loading at the end of the test is reported in Fig. 16(d). The presence of dimples at smaller scale, see Fig. 16(f), confirmed the nature of the fracture. In Fig. 16(d), unfused powder particles are visible inside the fracture surface, indicating the presence of lack of fusion defect.

In the same way as the node in Fig. 16(c), some cells were likely fractured only by fatigue damage. The absence of an overload zone with dimples in the case of tension–compression was also noticed by Lietaert et al. [34]. Similarly, Yang et al. stated that this distinct morphology is due to the redistribution of stresses to the adjacent cells [29]. The same authors also indicate that fracture features related to shear sliding and torsion were seen in some surfaces, leading to a complex fracture morphology. In the present work, such features are less evident, though the fracture morphology differs from that typical found in loading mode I only. Some hints of the propagation of cracks by shearing are identified in the fracture surface of the specimen tested at 1.2 % strain amplitude, as shown in Fig. 17(a). Another characteristic reported by Yang et al. is the presence of frictional grooves due to the cyclic contact between surfaces that were already separated. A similar characteristic is also found in the current study, as reported in Fig. 17(b), where some flattened faces are evident.

Fracture surfaces of the gyroid specimens tested at 0.5 % and 1.2 % strain amplitudes exhibited analogous characteristics despite the difference in the imposed strain level. The same reason explained for the case of FBCCZ specimens can be extended to the gyroid structure.

4. Conclusion

Specimens with a strut-based (FBCCZ) and a TPMS-based (skeletal-gyroid) cellular structure made of AISI 316L steel were manufactured by L-PBF. Assessment of the geometry and dimensions of the produced specimens proved the quality of the process. Axial tension–compression fatigue tests in strain control were carried out at different strain amplitudes to investigate the cyclic elastoplastic response and low cycle fatigue behaviour of these materials for the first time.

The outcomes of the present experimental campaign are summarised as follows:

- The cyclic elastoplastic response highlights a stiffer behaviour and higher maximum stresses of the FBCCZ as compared with the TPMS structure, alike the quasi-static properties. Both the cellular materials experienced a fast cyclic hardening in the first five cycles, followed by a cyclic softening, similar to what observed for the analogous bulk material tested in a previous study of the authors. Differently from the base (bulk) material, cellular materials suffered from a predominant linear cyclic softening. The linear cyclic softening, which dominates the fatigue life, is correlated with a decreasing tensile elastic modulus. Such a linear cyclic softening is thought to be caused by the progressive initiation and propagation of microcracks, as seen from the fractographic analysis showing multiple crack initiation sites.
- The characteristic morphology of the gyroid lattice structure ensured a more even distribution of stresses and strains which turned out to provide a substantially better low cycle fatigue strength than the FBCCZ, which is instead weakened by the presence of sharp notches (stress raisers). The gyroid cellular material approaches the strain-life curve of the base material, whereas the fatigue life of FBCCZ is one order of magnitude lower at a specified strain amplitude.

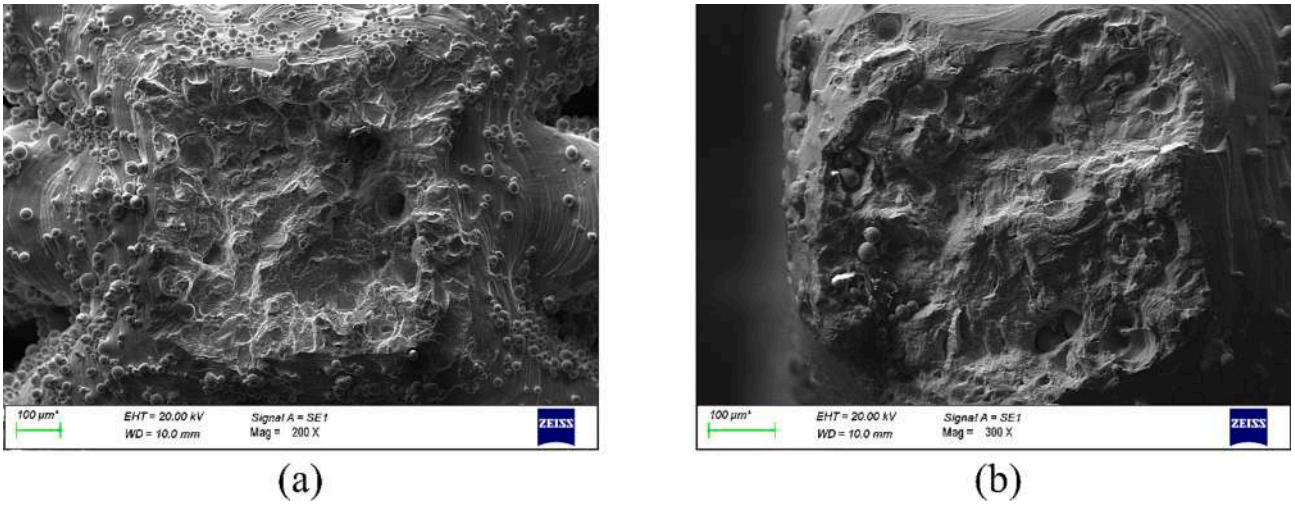

Fig. 15. Fracture surfaces of the FBCCZ specimen tested at 0.7 % strain amplitude: (a) internal node with multiple crack nucleation sites along the free surface and (b) corner node with an irregular fracture morphology and several pores with unfused powder particles.

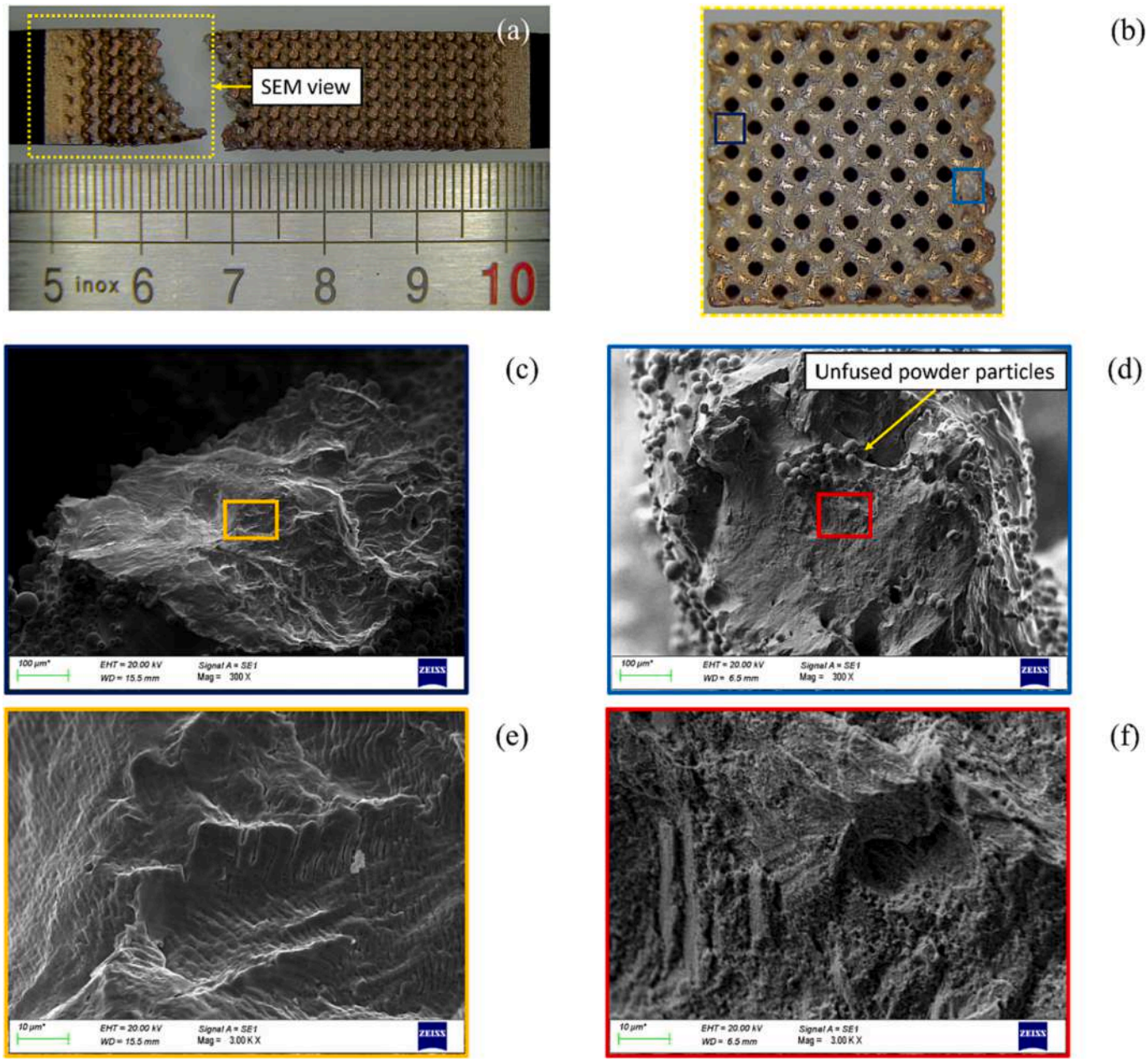

Fig. 16. Fractographic analysis of the gyroid specimen tested at 0.5 % strain amplitude: (a) side view of the broken specimen and (b) macroscopic top view of the fracture surface; (c) fracture surface of a cell in the left edge slightly inclined respect to the loading direction clearly showing (e) fatigue striations at lower scales; (d) fracture surface of a cell in the right edge failed by ductile damage showing a (f) rough morphology.

- Fractographic analysis reveals that FBCCZ structures failed at the nodes between two rows of cells, showing a planar fracture surface. On the other hand, gyroid specimens exhibited fracture surfaces that extended on more than one row. Clear signs of fatigue crack propagation are visible on most surfaces, whereas cells with ductile fracture morphology are rare. Dross near downward-facing walls, high surface roughness and gas or keyhole pores are identified as crack nucleation sites and might play a role in the reduction of the total fatigue life.

In conclusion, these results suggest that the skeletal-gyroid cellular material is to be preferred for structural applications in which cyclic strain is imposed, in the low cycle fatigue regime. While the FBCCZ lattice material is better suited for static loading conditions, particularly when high stiffness is sought.

CRediT authorship contribution statement

Marco Pelegatti: Conceptualization, Methodology, Formal analysis, Investigation, Writing – original draft. **Federico Scalzo:** Methodology, Formal analysis, Investigation, Validation, Writing – original draft. **Francesco Sordetti:** Methodology, Formal analysis, Investigation, Validation, Writing – review & editing. **Emanuele Vaglio:** Methodology, Formal analysis, Investigation, Writing – original draft. **Michele Magnan:** Formal analysis, Investigation. **Giovanni Totis:** Writing – review & editing, Supervision. **Marco Sortino:** Resources, Writing – review & editing, Supervision, Funding acquisition. **Denis Benasciutti:** Writing – review & editing, Supervision. **Alex Lanzutti:** Resources, Writing – review & editing, Supervision. **Francesco De Bona:** Conceptualization, Writing – review & editing, Supervision, Funding acquisition. **Enrico Salvati:** Conceptualization, Writing – review & editing, Supervision.

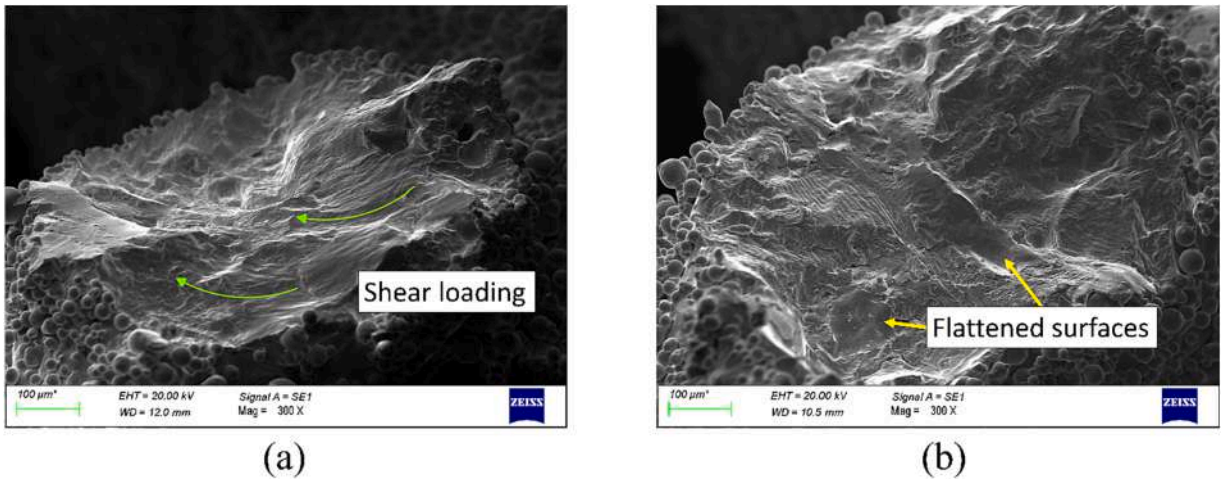

Fig. 17. Fracture surfaces of the gyroid specimen tested at 1.2 % strain amplitude: (a) frictional grooves due to shear loading acting on the surfaces and (b) flattened surfaces due to compression loading on split surfaces.

Declaration of Competing Interest

The authors declare that they have no known competing financial interests or personal relationships that could have appeared to influence the work reported in this paper.

Data availability

Data will be made available on request.

Acknowledgements

This study was carried out within the Interconnected Nord-Est Innovation Ecosystem (iNEST) and received funding from the European Union Next-GenerationEU (PIANO NAZIONALE DI RIPRESA E RESILIENZA (PNRR) – MISSIONE 4 COMPONENTE 2, INVESTIMENTO 1.5 – D.D. 1058 23/06/2022, ECS00000043). This manuscript reflects only the authors' views and opinions, neither the European Union nor the European Commission can be considered responsible for them. E. V. is grateful for funding under the REACT EU Italian PON 2014–2020 Program – Action IV.4 – Innovation (DM 1062, 10/08/2021). The Laboratory for Advanced Mechatronics (LAMA FVG) of the University of Udine is gratefully acknowledged. LAMA FVG is supported by the Universities of Udine, Trieste and SISSA, Regione Friuli-Venezia Giulia (Italy) and Italian Ministry of University and Research.

References

[1] Gibson L, Ashby M. Cellular Solids: Structure and Properties. 2nd ed. Cambridge: Cambridge University Press; 1997. Doi: 10.1017/CBO9781139878326.
[2] Tamburrino F, Graziosi S, Bordegoni M. The design process of additively manufactured mesoscale lattice structures: a review. J Comput Inf Sci Eng 2018;18:040801. https://doi.org/10.1115/1.4040131.
[3] Zok FW, Latture RM, Begley MR. Periodic truss structures. J Mech Phys Solids 2016;96:184–203. https://doi.org/10.1016/j.jmps.2016.07.007.
[4] Al-Ketan O, Abu Al-Rub RK. Multifunctional mechanical metamaterials based on triply periodic minimal surface lattices. Adv Eng Mater 2019;21:1900524. https://doi.org/10.1002/adem.201900524.
[5] Du Plessis A, Razavi SMJ, Benedetti M, Murchio S, Leary M, Watson M, et al. Properties and applications of additively manufactured metallic cellular materials: A review. Prog Mater Sci 2022;125:100918. https://doi.org/10.1016/j.pmatsci.2021.100918.
[6] Ozdemir Z, Hernandez-Nava E, Tyas A, Warren JA, Fay SD, Goodall R, et al. Energy absorption in lattice structures in dynamics: Experiments. Int J Impact Eng 2016;89:49–61. https://doi.org/10.1016/j.ijimpeng.2015.10.007.
[7] Yin H, Zhang W, Zhu L, Meng F, Liu J, Wen G. Review on lattice structures for energy absorption properties. Compos Struct 2022;304:116397. https://doi.org/10.1016/j.compstruct.2022.116397.
[8] Scalzo F, Totis G, Vaglio E, Sortino M. Passive chatter suppression of thin-walled parts by means of high-damping lattice structures obtained from selective laser melting. J Manuf Mater Process 2020;4:117. https://doi.org/10.3390/jmmp4040117.
[9] Scalzo F, Totis G, Vaglio E, Sortino M. Experimental study on the high-damping properties of metallic lattice structures obtained from SLM. Precis Eng 2021;71:63–77. https://doi.org/10.1016/j.precisioneng.2021.02.010.
[10] Scalzo F, Totis G, Sortino M. Influence of the experimental setup on the damping properties of SLM lattice structures. Exp Mech 2023;63:15–28. https://doi.org/10.1007/s11340-022-00898-8.
[11] Zhu L, Li N, Childs PRN. Light-weighting in aerospace component and system design. Propuls Power Res 2018;7:103–19. https://doi.org/10.1016/j.jppr.2018.04.001.
[12] Vaneker T, Bernard A, Moroni G, Gibson I, Zhang Y. Design for additive manufacturing: Framework and methodology. CIRP Ann 2020;69(2):578–99.
[13] Jafari D, Wits WW. The utilization of selective laser melting technology on heat transfer devices for thermal energy conversion applications: A review. Renew Sustain Energy Rev 2018;91:420–42. https://doi.org/10.1016/j.rser.2018.03.109.
[14] Zhang XZ, Leary M, Tang HP, Song T, Qian M. Selective electron beam manufactured Ti-6Al-4V lattice structures for orthopedic implant applications: Current status and outstanding challenges. Curr Opin Solid State Mater Sci 2018;22:75–99. https://doi.org/10.1016/j.cossms.2018.05.002.
[15] Aslan B, Yıldız AR. Optimum design of automobile components using lattice structures for additive manufacturing. Mater Test 2020;62:633–9. https://doi.org/10.3139/120.111527.
[16] Blakey-Milner B, Gradl P, Snedden G, Brooks M, Pitot J, Lopez E, et al. Metal additive manufacturing in aerospace: A review. Mater Des 2021;209:110008. https://doi.org/10.1016/j.matdes.2021.110008.
[17] Nafis BM, Whitt R, Iradukunda AC, Huitink D. Additive manufacturing for enhancing thermal dissipation in heat sink implementation: a review. Heat Transf Eng 2021;42:967–84. https://doi.org/10.1080/01457632.2020.1766246.
[18] Mazur M, Leary M, Sun S, Vcelka M, Shidid D, Brandt M. Deformation and failure behaviour of Ti-6Al-4V lattice structures manufactured by selective laser melting (SLM). Int J Adv Manuf Technol 2016;84:1391–411. https://doi.org/10.1007/s00170-015-7655-4.
[19] Zhang L, Feih S, Daynes S, Chang S, Wang MY, Wei J, et al. Energy absorption characteristics of metallic triply periodic minimal surface sheet structures under compressive loading. Addit Manuf 2018;23:505–15. https://doi.org/10.1016/j.addma.2018.08.007.
[20] Molavitabrizi D, Bengtsson R, Botero C, Rännar LE, Mousavi SM. Damage-induced failure analysis of additively manufactured lattice materials under uniaxial and multiaxial tension. Int J Solids Struct 2022;252:111783. https://doi.org/10.1016/j.ijsolstr.2022.111783.
[21] Yánez A, Cuadrado A, Martel O, Afonso H, Monopoli D. Gyroid porous titanium structures: A versatile solution to be used as scaffolds in bone defect reconstruction. Mater Des 2018;140:21–9. https://doi.org/10.1016/j.matdes.2017.11.050.
[22] Gümrük R, Mines RAW, Karadeniz S. Static mechanical behaviours of stainless steel micro-lattice structures under different loading conditions. Mater Sci Eng A 2013;586:392–406. https://doi.org/10.1016/j.msea.2013.07.070.

[23] Maconachie T, Leary M, Lozanovski B, Zhang X, Qian M, Faruque O, et al. SLM lattice structures: Properties, performance, applications and challenges. Mater Des 2019;183:108137. https://doi.org/10.1016/j.matdes.2019.108137.
[24] Cutolo A, Engelen B, Desmet W, Van Hooreweder B. Mechanical properties of diamond lattice Ti–6Al–4V structures produced by laser powder bed fusion: On the effect of the load direction. J Mech Behav Biomed Mater 2020;104:103656. https://doi.org/10.1016/j.jmbbm.2020.103656.
[25] Barber H, Kelly CN, Nelson K, Gall K. Compressive anisotropy of sheet and strut based porous Ti–6Al–4V scaffolds. J Mech Behav Biomed Mater 2021;115:104243. https://doi.org/10.1016/j.jmbbm.2020.104243.
[26] Zhao S, Li SJ, Hou WT, Hao YL, Yang R, Misra RDK. The influence of cell morphology on the compressive fatigue behavior of Ti-6Al-4V meshes fabricated by electron beam melting. J Mech Behav Biomed Mater 2016;59:251–64. https://doi.org/10.1016/j.jmbbm.2016.01.034.
[27] Wu MW, Chen JK, Lin BH, Chiang PH, Tsai MK. Compressive fatigue properties of additive-manufactured Ti-6Al-4V cellular material with different porosities. Mater Sci Eng A 2020;790:139695. https://doi.org/10.1016/j.msea.2020.139695.
[28] Boniotti L, Beretta S, Patriarca L, Rigoni L, Foletti S. Experimental and numerical investigation on compressive fatigue strength of lattice structures of AlSi7Mg manufactured by SLM. Int J Fatigue 2019;128:105181. https://doi.org/10.1016/j.ijfatigue.2019.06.041.
[29] Yang L, Wu S, Yan C, Chen P, Zhang L, Han C, et al. Fatigue properties of Ti-6Al-4V Gyroid graded lattice structures fabricated by laser powder bed fusion with lateral loading. Addit Manuf 2021;46:102214. https://doi.org/10.1016/j.addma.2021.102214.
[30] Dallago M, Fontanari V, Torresani E, Leoni M, Pederzolli C, Potrich C, et al. Fatigue and biological properties of Ti-6Al-4V ELI cellular structures with variously arranged cubic cells made by selective laser melting. J Mech Behav Biomed Mater 2018;78:381–94. https://doi.org/10.1016/j.jmbbm.2017.11.044.
[31] Köhnen P, Haase C, Bültmann J, Ziegler S, Schleifenbaum JH, Bleck W. Mechanical properties and deformation behavior of additively manufactured lattice structures of stainless steel. Mater Des 2018;145:205–17. https://doi.org/10.1016/j.matdes.2018.02.062.
[32] Boniotti L, Dancette S, Gavazzoni M, Lachambre J, Buffiere JY, Foletti S. Experimental and numerical investigation on fatigue damage in micro-lattice materials by Digital Volume Correlation and μCT-based finite element models. Eng Fract Mech 2022;266:108370. https://doi.org/10.1016/j.engfracmech.2022.108370.
[33] Falkowska A, Seweryn A. Fatigue of titanium alloy Ti6Al4V with diamond structure obtained by Laser Power Bed Fusion method. Int J Fatigue 2022;163:107079. https://doi.org/10.1016/j.ijfatigue.2022.107079.
[34] Lietaert K, Cutolo A, Boey D, Van Hooreweder B. Fatigue life of additively manufactured Ti6Al4V scaffolds under tension-tension, tension-compression and compression-compression fatigue load. Sci Rep 2018;8:4957. https://doi.org/10.1038/s41598-018-23414-2.
[35] Gavazzoni M, Beretta S, Foletti S. Response of an aluminium Schwarz triply periodic minimal surface lattice structure under constant amplitude and random fatigue. Int J Fatigue 2022;163:107020. https://doi.org/10.1016/j.ijfatigue.2022.107020.
[36] Li Y, Attallah MM, Coules H, Martinez R, Pavier M. Fatigue of octet-truss lattices manufactured by Laser Powder Bed Fusion. Int J Fatigue 2023;170:107524. https://doi.org/10.1016/j.ijfatigue.2023.107524.
[37] Tomažinčič D, Nečemer B, Vesenjak M, Klemenc J. Low-cycle fatigue life of thin-plate auxetic cellular structures made from aluminium alloy 7075–T651. Fatigue Fract Eng Mater Struct 2019;42:1022–36. https://doi.org/10.1111/ffe.12966.
[38] Tomažinčič D, Vesenjak M, Klemenc J. Prediction of static and low-cycle durability of porous cellular structures with positive and negative Poisson's ratios. Theor Appl Fract Mech 2020;106:102479. https://doi.org/10.1016/j.tafmec.2020.102479.
[39] Molavitabrizi D, Ekberg A, Mousavi SM. Computational model for low cycle fatigue analysis of lattice materials: Incorporating theory of critical distance with elastoplastic homogenization. Eur J Mech A Solids 2022;92:104480. https://doi.org/10.1016/j.euromechsol.2021.104480.
[40] Mozafari F, Temizer I. Computational homogenization of fatigue in additively manufactured microlattice structures. Comput Mech 2023;71:367–84. https://doi.org/10.1007/s00466-022-02243-1.
[41] Zhang P, Zhang DZ, Zhong B. Constitutive and damage modelling of selective laser melted Ti-6Al-4V lattice structure subjected to low cycle fatigue. Int J Fatigue 2022;159:106800. https://doi.org/10.1016/j.ijfatigue.2022.106800.
[42] Yu CH, Leicht A, Peng RL, Moverare J. Low cycle fatigue of additively manufactured thin-walled stainless steel 316L. Mater Sci Eng A 2021;821:141598. https://doi.org/10.1016/j.msea.2021.141598.
[43] Pelegatti M, Benasciutti D, De Bona F, Lanzutti A, Magnan M, Novak JS, et al. On the factors influencing the elastoplastic cyclic response and low cycle fatigue failure of AISI 316L steel produced by laser-powder bed fusion. Int J Fatigue 2022;165:107224. https://doi.org/10.1016/j.ijfatigue.2022.107224.
[44] Beard W, Lancaster R, Barnard N, Jones T, Adams J. The influence of surface finish and build orientation on the low cycle fatigue behaviour of laser powder bed fused stainless steel 316L. Mater Sci Eng A 2023;864:144593. https://doi.org/10.1016/j.msea.2023.144593.
[45] Man J, Blinn B, Šulák I, Kuběna I, Smaga M, Chlup Z, et al. Formation of deformation induced martensite in fatigued 316L steels manufactured by selective laser melting (SLM). Procedia Struct Integr 2023;43:203–8. https://doi.org/10.1016/j.prostr.2022.12.259.
[46] Agius D, Kourousis KI, Wallbrink C, Song T. Cyclic plasticity and microstructure of as-built SLM Ti-6Al-4V: The effect of build orientation. Mater Sci Eng A 2017;701:85–100. https://doi.org/10.1016/j.msea.2017.06.069.
[47] Zhang P, He AN, Liu F, Zhang K, Jiang J, Zhang DZ. Evaluation of low cycle fatigue performance of selective laser melted titanium alloy Ti–6Al–4V. Metals 2019;9:1041. https://doi.org/10.3390/met9101041.
[48] Gribbin S, Bicknell J, Jorgensen L, Tsukrov I, Knezevic M. Low cycle fatigue behavior of direct metal laser sintered Inconel alloy 718. Int J Fatigue 2016;93:156–67. https://doi.org/10.1016/j.ijfatigue.2016.08.019.
[49] Sausto F, Marchese G, Bassini E, Calandri M, Biamino S, Ugues D, et al. Anisotropic mechanical and fatigue behaviour of Inconel718 produced by SLM in LCF and high-temperature conditions. Fatigue Fract Eng Mater Struct 2021;44:271–92. https://doi.org/10.1111/ffe.13373.
[50] Tsopanos S, Mines RAW, McKown S, Shen Y, Cantwell WJ, Brooks W, et al. The influence of processing parameters on the mechanical properties of selectively laser melted stainless steel microlattice structures. J Manuf Sci Eng 2010;132:041011. https://doi.org/10.1115/1.4001743.
[51] Yan C, Hao L, Hussein A, Young P, Raymont D. Advanced lightweight 316L stainless steel cellular lattice structures fabricated via selective laser melting. Mater Des 2014;55:533–41. https://doi.org/10.1016/j.matdes.2013.10.027.
[52] Alsalla H, Hao L, Smith C. Fracture toughness and tensile strength of 316L stainless steel cellular lattice structures manufactured using the selective laser melting technique. Mater Sci Eng A 2016;669:1–6. https://doi.org/10.1016/j.msea.2016.05.075.
[53] Prashanth KG, Löber L, Klauss HJ, Kühn U, Eckert J. Characterization of 316L steel cellular dodecahedron structures produced by selective laser melting. Technologies 2016;4:34. https://doi.org/10.3390/technologies4040034.
[54] Zhong T, He K, Li H, Yang L. Mechanical properties of lightweight 316L stainless steel lattice structures fabricated by selective laser melting. Mater Des 2019;181:108076. https://doi.org/10.1016/j.matdes.2019.108076.
[55] Zhang C, Zheng H, Yang L, Li Y, Jin J, Cao W, et al. Mechanical responses of sheet-based gyroid-type triply periodic minimal surface lattice structures fabricated using selective laser melting. Mater Des 2022;214:110407. https://doi.org/10.1016/j.matdes.2022.110407.
[56] Deshpande VS, Ashby MF, Fleck NA. Foam topology: bending versus stretching dominated architectures. Acta Mater 2001;49:1035–40. https://doi.org/10.1016/S1359-6454(00)00379-7.
[57] Leary M, Mazur M, Elambasseril J, McMillan M, Chirent T, Sun Y, et al. Selective laser melting (SLM) of AlSi12Mg lattice structures. Mater Des 2016;98:344–57. https://doi.org/10.1016/j.matdes.2016.02.127.
[58] Rajagopalan S, Robb RA. Schwarz meets Schwann: design and fabrication of biomorphic and durataxic tissue engineering scaffolds. Med Image Anal 2006;10:693–712. https://doi.org/10.1016/j.media.2006.06.001.
[59] Von Schnering HG, Nesper R. Nodal surfaces of Fourier series: fundamental invariants of structured matter. Z Phys B Condensed Matter 1991;83:407–12. https://doi.org/10.1007/BF01313411.
[60] Yang L, Yan C, Fan H, Li Z, Cai C, Chen P, et al. Investigation on the orientation dependence of elastic response in Gyroid cellular structures. J Mech Behav Biomed Mater 2019;90:73–85. https://doi.org/10.1016/j.jmbbm.2018.09.042.
[61] Drücker S, Inman S, Fiedler B, (2018). Simulation and optimization of the load introduction geometry of additively manufactured lattice structure specimens. In *ECCM 2018-18th European Conference on Composite Materials*.
[62] Andrews EW, Gioux G, Onck P, Gibson LJ. Size effects in ductile cellular solids. Part II: experimental results. Int J Mech Sci 2001;43:701–13. https://doi.org/10.1016/S0020-7403(00)00043-6.
[63] Pelegatti M, Benasciutti D, De Bona F, Salvati E. Experimental characterization and modelling of cyclic elastoplastic response of an AISI 316L steel lattice structure produced by laser-powder bed fusion. Procedia Struct Integr 2023;47:238–46. https://doi.org/10.1016/j.prostr.2023.07.101.
[64] Pelegatti M, Benasciutti D, De Bona F, Lanzutti A, Novak JS, Salvati E. Strain-controlled fatigue loading of an additively manufactured AISI 316L steel: Cyclic plasticity model and strain–life curve with a comparison to the wrought material. Fatigue Fract Eng Mater Struct 2023;46:2195–211. https://doi.org/10.1111/ffe.13992.
[65] Lorenzon A, Vaglio E, Casarsa L, Sortino M, Totis G, Saragò G, et al. Heat transfer and pressure loss performances for additively manufactured pin fin arrays in annular channels. Appl Therm Eng 2022;202:117851. https://doi.org/10.1016/j.applthermaleng.2021.117851.

[66] Ashby MF, Evans T, Fleck NA, Hutchinson JW, Wadley HNG, Gibson LJ. Metal foams: a design guide. Elsevier 2000. https://doi.org/10.1016/B978-0-7506-7219-1.X5000-4.
[67] Sugimura Y, Rabiei A, Evans AG, Harte AM, Fleck NA. Compression fatigue of a cellular Al alloy. Mater Sci Eng A 1999;269:38–48. https://doi.org/10.1016/S0921-5093(99)00147-1.
[68] Li SJ, Murr LE, Cheng XY, Zhang ZB, Hao YL, Yang R, et al. Compression fatigue behavior of Ti–6Al–4V mesh arrays fabricated by electron beam melting. Acta Mater 2012;60:793–802. https://doi.org/10.1016/j.actamat.2011.10.051.
[69] Liu YJ, Wang HL, Li SJ, Wang SG, Wang WJ, Hou WT, et al. Compressive and fatigue behavior of beta-type titanium porous structures fabricated by electron beam melting. Acta Mater 2017;126:58–66. https://doi.org/10.1016/j.actamat.2016.12.052.
[70] Dowling NE. Geometry effects and the J-integral approach to elastic-plastic fatigue crack growth. In: Cracks and fracture, ASTM International. pp. 19–32. 1976.
[71] Salvati E, Sui T, Zhang H, Lunt AJ, Fong KS, Song X, et al. Elucidating the mechanism of fatigue crack acceleration following the occurrence of an underload. Adv Eng Mater 2016;18:2076–87. https://doi.org/10.1002/adem.201600069.
[72] Dowling NE. Mechanical Behavior of Materials Engineering Methods for Deformation, Fracture, and Fatigue. 4th ed. Harlow: Pearson Education; 2013.
[73] Manson SS, Halford GR. Fatigue and Durability of Structural Materials. Materials Park: ASM International; 2006.
[74] Kelly CN, Kahra C, Maier HJ, Gall K. Processing, structure, and properties of additively manufactured titanium scaffolds with gyroid-sheet architecture. Addit Manuf 2021;41:101916. https://doi.org/10.1016/j.addma.2021.101916.
[75] Ashouri D, Voshage M, Burkamp K, Kunz J, Bezold A, Schleifenbaum JH, et al. Mechanical behaviour of additive manufactured 316L f2ccz lattice structure under static and cyclic loading. Int J Fatigue 2020;134:105503. https://doi.org/10.1016/j.ijfatigue.2020.105503.
[76] Echeta I, Feng X, Dutton B, Leach R, Piano S. Review of defects in lattice structures manufactured by powder bed fusion. Int J Adv Manuf Technol 2020;106:2649–68. https://doi.org/10.1007/s00170-019-04753-4.